Naval Research Laboratory

AD-A198 360

Momentum Flux Increases and Coherent-Structure Dynamics in a Subsonic Axisymmetric Free Jet

F. F. GRINSTEIN, F. HUSSAIN* AND E. S. ORAN

Laboratory for Computational Physics and Fluid Dynamics

**Department of Mechanical Engineering
University of Houston*

August 19, 1988

88 9 14 206

REPORT DOCUMENTATION PAGE

Form Approved
OMB No 0704-0188

1a. REPORT SECURITY CLASSIFICATION	1b. RESTRICTIVE MARKINGS
UNCLASSIFIED	

2a. SECURITY CLASSIFICATION AUTHORITY	3. DISTRIBUTION / AVAILABILITY OF REPORT
2b. DECLASSIFICATION / DOWNGRADING SCHEDULE	Approved for public release; distribution unlimited.

4. PERFORMING ORGANIZATION REPORT NUMBER(S)	5. MONITORING ORGANIZATION REPORT NUMBER(S)
NRL Memorandum Report 6279	

6a. NAME OF PERFORMING ORGANIZATION	6b. OFFICE SYMBOL (If applicable)	7a. NAME OF MONITORING ORGANIZATION
Naval Research Laboratory	Code 4410	Office of Naval Research

6c. ADDRESS (City, State, and ZIP Code)	7b. ADDRESS (City, State, and ZIP Code)
Washington, DC 20375-5000	800 N. Quincy Street Arlington, VA 22217-5000

8a. NAME OF FUNDING / SPONSORING ORGANIZATION	8b. OFFICE SYMBOL (If applicable)	9. PROCUREMENT INSTRUMENT IDENTIFICATION NUMBER
Office of Naval Research		

8c. ADDRESS (City, State, and ZIP Code)	10. SOURCE OF FUNDING NUMBERS			
800 N. Quincy Street Arlington, VA 22217-5000	PROGRAM ELEMENT NO.	PROJECT NO.	TASK NO	WORK UNIT ACCESSION NO.
	61153N	44-169208	RR024-03-01	DN155-117

11. TITLE (Include Security Classification)

Momentum Flux Increases and Coherent-Structure Dynamics in a Subsonic Axisymmetric Free Jet

12. PERSONAL AUTHOR(S)
Grinstein, F. F., Hussain,* F. and Oran, E. S.

13a. TYPE OF REPORT	13b. TIME COVERED		14. DATE OF REPORT (Year, Month, Day)	15 PAGE COUNT
Interim	FROM 6/87	TO Present	1988 August 19	54

16. SUPPLEMENTARY NOTATION

*Department of Mechanical Engineering, University of Houston

17.	COSATI CODES		18. SUBJECT TERMS (Continue on reverse if necessary and identify by block number)
FIELD	GROUP	SUB-GROUP	Coherent structures ; Compressible free shear flows ;
			Subsonic free jets .

19. ABSTRACT (Continue on reverse if necessary and identify by block number)

The spatial evolution of a high Reynolds number, axisymmetric free jet is computed numerically with a compressible, two-dimensional, finite-difference Flux-Corrected Transport algorithm and appropriate inflow and outflow boundary conditions. The simulated flow fields are examined to obtain an insight into the physics of large-scale organized structures in the transition region and to investigate the effects of the initial conditions, Mach number and controlled axial excitation. Contrary to the traditionally accepted notion of isobaric free jet flow, the results show significant streamwise increases in the momentum flux — consistent with previously recorded experimental data. The results are discussed in terms of instantaneous velocity, vorticity and pressure fields.

20. DISTRIBUTION / AVAILABILITY OF ABSTRACT	21 ABSTRACT SECURITY CLASSIFICATION
☒ UNCLASSIFIED/UNLIMITED ☐ SAME AS RPT ☐ DTIC USERS	UNCLASSIFIED

22a. NAME OF RESPONSIBLE INDIVIDUAL	22b. TELEPHONE (Include Area Code)	22c. OFFICE SYMBOL
Fernando F. Grinstein	202/767-6583	Code 4410

DD Form 1473, JUN 86

Previous editions are obsolete.

SECURITY CLASSIFICATION OF THIS PAGE

CONTENTS

Accession For

NTIS GRA&I	☒
DTIC TAB	☐
Unannounced	☐
Justification	

By_____

Distribution/

Availability Codes

Dist	Avail and/or Special
A-1	

DTIC
COPY
INSPECTED
1

MOMENTUM FLUX INCREASES AND COHERENT-STRUCTURE DYNAMICS IN A SUBSONIC AXISYMMETRIC FREE JET

1. INTRODUCTION

Numerical investigations have been used to study both planar and axisymmetric shear layers. A number of these have modeled temporally developing mixing layers (Patnaik et al. 1976; Riley & Metcalfe 1980; Moin et al. 1985). Others have modeled spatially developing layers (Ashurst 1979; Davis & Moore 1985; Grinstein et al. 1986), which use inflow and outflow boundary conditions and therefore correspond more closely to the physical situations.

Only in very few cases have the simulated flows been compared to experimental data to enhance our basic understanding of large-scale organized structures and turbulence physics. One such study involving direct numerical simulations of the plane mixing layer using spectral methods (Metcalfe et al. 1987) shows good agreement with experimental data on educed coherent vorticity, strain rate and production, in spite of the clear differences between the simulated and measured flows: the simulations addressed a spatially periodic temporally developing transitional mixing layer, while the laboratory measurements were made in a spatially evolving, temporally stationary mixing layer of a much higher Reynolds number.

Recent numerical simulations of unforced, subsonic, compressible, spatially evolving two-dimensional shear layers have shown a number of important features of the flow field in the transition region (Grinstein et al. 1986, 1987). The calculated distribution of merging locations (Grinstein et al. 1987) was in good agreement with the experimental distributions obtained with weakly excited axisymmetric (Zaman & Hussain 1977; Kibens 1979) shear layers. The results indicated that the presence of an underlying degree of organization in unforced two-dimensional shear layers is a result of upstream feedback of perturbations caused by downstream vortex interactions.

This paper represents an experimental-numerical collaboration, prompted by the experimental result that the momentum flux in a jet was found to increase in the downstream direction (Clark 1974; Hussain & Clark 1977), contrary to traditional expectations. The results and interpretations presented here are not only a successful result of the collaboration but are also a clear evidence of the crucial role of computer simulations in answering questions which experiments alone can not

easily answer. We strongly feel that such collaboration between the two complementary approaches is necessary for understanding the physics of turbulence. In this paper we investigate the validity of the traditional hypothesis of isobaric free jet flow. It is usually assumed that the mean static pressure gradients in a free jet are everywhere negligibly small compared to other mean forces on the fluid. Thus the pressure in a jet is considered virtually constant and equal to the ambient pressure (Abramovich 1963). As a consequence of this hypothesis, the mean longitudinal momentum flux should be a constant at each streamwise station. Historically, the momentum flux in a free jet has been considered a fundamental invariant. In fact, free jet data which failed to show constancy of momentum flux were generally rejected as unreliable (e.g., Mons et al. 1971; Kline et al. 1973).

In the experimental study of planar jets by Hussain & Clark (1977), the streamwise momentum flux was computed from velocity data measured with hot wires. It was found that the momentum flux increases in the streamwise direction, and that the extent of the increase depends on the initial conditions. They also noted that pressure can drop considerably within the turbulent regions of a free jet because of transverse turbulent fluctuations. Although they measured decreases in the static pressure that were consistent with the observed increases in the momentum flux, they could not obtain the required quantitative balances between the integrated pressure and momentum flux from the experimental data. This was attributed to large uncertainties in both velocity and pressure measurements due to effects of high turbulence levels in the jet, especially at its outer edges, on both hot wires and pitot-static-pressure probes. So, while the streamwise increase in the momentum flux in a free jet was asserted by the authors, the accuracy of the measured increase in the momentum flux and of the measured dependence of this increase on the initial conditions remained unresolved.

Here we use time-dependent spatially evolving simulations of shear flows to study the transition region of a subsonic, compressible, axisymmetric free jet at high Reynolds number. In addition to having the advantage of providing spatial distributions of the instantaneous flow field, a computer simulation also has the advantage of being free from the effect of probe interference and the highly restrictive Taylor's hypothesis. The computations have also the advantage of being free from the effects of high turbulence level and flow reversal on hot wire measurements, both effects character-istic of outer regions of free jet flows. The calculations show that negative (i.e., countergradient) production occurs in regions where the axis of an inclined structure or the line connecting the cen-ters of two merging structures has the same slope as the mean velocity profile (Hussain 1983). This was observed in laboratory experiments with plane mixing layers subject to appropriate forcing (Oster & Wygnanski 1982), and in axisymmetric jets (Zaman & Hussain 1977, 1980) in the region immediately downstream of an induced localized merging. We particularly focus on the question of whether the momentum flux in a free jet flow remains constant. The calculations indicate that the mean static pressure drops significantly within the jet, accounting for the growth in the streamwise

momentum flux and supporting the experimental results. We also describe the spatial features of time-dependent velocity, vorticity and pressure fields associated with coherent structures in the jet and discuss their dependence on controlled excitation.

2. THE NUMERICAL MODEL

The physical system we simulate is a compressible axisymmetric free jet of air emerging into quiescent ambient air. The initially laminar jet has a top hat axial velocity profile at the exit and uniform standard temperature and pressure everywhere. The Mach number is in the range 0.43–0.57, the free-stream velocity, U_o, is 1.5–2.0 × 10⁴ cm/s, and the diameter, D, is 1.4 cm. The flow system is shown schematically in figure 1. These are idealized initial conditions since most laboratory jets at similar Mach numbers are not initially laminar. The jets considered here are nearly incompressible, to the extent that the turbulence Mach number is very small. At the same time, the Reynolds number and the Mach number for the fast-free-flow regimes considered are high enough to enable their optimal study with an inviscid, explicit, finite-difference numerical model such as discussed below.

The numerical model used to perform the simulations consists of the two-dimensional, time-dependent inviscid conservation equations for mass, momentum, and energy density for an ideal gas:

$$\frac{\partial \rho}{\partial t} = -\nabla \cdot (\rho \mathbf{V}), \tag{1}$$

$$\frac{\partial (\rho \mathbf{V})}{\partial t} = -\nabla \cdot (\rho \mathbf{V}\mathbf{V}) - \nabla P, \tag{2}$$

$$\frac{\partial E}{\partial t} = -\nabla \cdot (E\mathbf{V}) - \nabla \cdot P\mathbf{V}. \tag{3}$$

Here $E = P/(\gamma - 1) + (1/2)\rho V^2$ is the total energy and $\mathbf{V}$, P, ρ, and γ, are the fluid velocity, pressure, mass density, and the ratio of specific heats, respectively.

The equations are solved using the nonlinear, high-order, explicit, compressible finite-difference Flux-Corrected Transport (FCT) algorithm (Boris and Book 1976). Through a two-step predictor-corrector scheme, FCT ensures that all conserved quantities remain monotonic and positive. First, it modifies the linear properties of a high-order algorithm by adding diffusion during convective transport to prevent dispersive ripples from arising. The added diffusion is then removed in an antidiffusion phase of the integration cycle. Hence, these calculations maintain the high order of accuracy without resorting to artificial viscosity to stabilize the algorithm.

In the present calculations the code FAST2D was used to solve equations 1–3. The code uses direction splitting and timestep splitting with a one-dimensional fourth-order phase-accurate FCT algorithm. The code FAST2D has been extensively tested and used in the last ten years (see details and references in Oran & Boris 1987). Applications to subsonic flows include calculations of vortex dynamics and asymmetric mixing in shear layers (Grinstein et al. 1986, 1987). The simulations of two-dimensional compressible shear-flows have reproduced the basic large-scale features of the flow observed in the laboratory experiments, e.g., the asymmetric entrainment (Grinstein et al. 1986), the distribution of merging locations (Grinstein et al. 1987), and the spreading rate of the mixing

4

layer (shown below in this paper). Much work has been done to test boundary conditions and convergence in FAST2D models. Boris et al. (1983, 1985) described tests of boundary conditions in both subsonic and supersonic flows, and Grinstein et al. (1986) described boundary-condition and resolution tests in subsonic and choked shear flows. In addition, Kailasanath et al. (1987) reported tests in the case of confined subsonic shear flows in axisymmetric ramjets.

No explicit subgrid turbulence model was included. However, there is an effective filter for high frequencies which is part of the nonlinearity of the FCT algorithm. The filter does not affect the large-scale structures, but ensures that wavelengths smaller than a few computational cells are numerically diffused. Thus, provided that the computational grid is chosen fine enough to resolve the large-scale features of the flow, the residual numerical viscosity of the algorithm mimics the behavior of physical viscosity at high Reynolds number by dumping small-scale structures on the order of a few computational cells. There are essentially no viscous effects at scales greater than four or five cells.

The ability of the nonlinear filter of the algorithm to simulate the effects of physical viscosity was verified, in particular, by a study of the laminar spread of a simulated mixing layer by Grinstein & Guirguis (1987) which will be reported in detail elsewhere. In this study the gridding and free stream velocities were the same as those in the present free jet flow configuration, but zero transverse velocity was enforced in the calculations. This condition (reasonable in the high Reynolds number limit, where $V_{transv}/V_{stream} = \mathcal{O}(1/Re)$) was enforced in order to ensure that the spread of the shear layer was strictly laminar and due only to the residual numerical viscosity of the algorithm. Then, by comparing the spread of the velocity profile from this calculation to that given by the full numerical solution of the corresponding incompressible laminar flow equation for a shear layer (e.g., Schlichting 1968), it was possible to obtain a bound on the effective numerical viscosity in the simulations. Using the bound on the effective numerical viscosity, and based on the jet velocity and diameter, the effective Reynolds number Re_D for the large-scale structures in the present simulations is greater than $\approx 1.5 \times 10^5$.

Inflow and outflow boundary conditions are used to represent the effects of the region outside of the computational domain. These boundary conditions should be as "transparent" as possible, which means that unphysical reflections or wave absorption at the boundaries should be minimal. Imposing such boundary conditions is difficult, since they generally require representing the flow field outside of the domain with a very restricted amount of information on the behavior of the solutions at the boundaries. Because of this difficulty, many previous simulations have used periodic boundary conditions to avoid the problem. Such temporally (as opposed to spatially) evolving calculations can be thought of as describing the time evolution of the flow in compact regions.

However, laboratory flows evolve both in space and time, and in addition to the limitations of transformation between spatially and temporally growing disturbances (Gaster 1962; Corcos 1980), the dynamics of spatially evolving turbulent shear flows cannot be captured by spatially periodic simulations.

The calculations presented below use inflow and outflow boundary conditions developed and tested for multidimensional FCT calculations (Boris et al. 1985; Grinstein et al. 1986, 1987). In order to compute derivatives at the boundaries of the computational domain, we define the behavior of physical variables at an extra row of guard cells surrounding the domain. This provides a way to model the behavior of the fluid near the boundaries in terms of what is expected of the flow field outside of the computational domain. In the calculations presented below, the inflow boundary conditions are:

$$\rho_g = \rho_{\text{inflow}}, \tag{4a}$$

$$v_g = v_{\text{inflow}}, \tag{4b}$$

$$P_g = P_1, \tag{4c}$$

where the subscripts g and 1 refer to the guard cells and to the first row of cells inside the computational domain (at the inflow), respectively. Thus the density and inflow velocity of the jet are specified and the energy at the inflow is determined from a zero-slope condition on pressure. This allows the pressure at the inflow to vary in response to acoustic waves generated by events downstream. An important result of allowing this feedback is that the instabilities can evolve naturally in the calculation, and they do not have to be driven continuously to be reinitiated.

The boundary conditions at the outflow guard cells define the density and velocity through zeroth- and first-order extrapolations from the last two cells:

$$\rho_g = \rho_n, \tag{5a}$$

$$v_g = 2v_n - v_{n-1}. \tag{5b}$$

These boundary conditions are consistent with fixing the inflow density and velocity of the jet. The energy at the outflow guard cells is defined in terms of the density and velocity given by eqs. (5a–b) and the pressure defined by

$$P_g = P_n + \frac{(Y_g - Y_n)}{(Y_g - Y_j)}(P_{amb} - P_n), \tag{5c}$$

where Y is either the radial or axial coordinate, and the subscript j refers to the location of the lip of the nozzle. Equation 5c is the result of interpolating between the pressure value at the boundary, P_n, and the ambient value at infinity, P_{amb}. It ensures that the pressure equals P_{amb} at an infinite distance from the nozzle. The slow relaxation of the pressure towards the known ambient value is necessary because the pressure at the inflow is not specified, but calculated from other variables.

By giving a reference pressure value we avoid secular errors in the calculations.

A more realistic transition to the flow region of interest downstream of the nozzle (the small dotted-box region in figure 1) is obtained by surrounding it with a buffer region and imposing the inflow and outflow boundary conditions on the outer boundaries of the computational domain. In addition, a portion of the nozzle is included inside the computational domain. The effectiveness of the inflow and outflow boundary conditions depends on the dimensions of the buffer region and depends inversely on the time interval over which the simulations are carried out. The effectiveness of the outflow boundary conditions is also somewhat dependent on the nature of the numerical dissipation at the boundaries which will determine how well spurious reflections will be damped there. The practical choice of the computational domain and the gridding was motivated by these considerations.

Figure 2 shows a schematic diagram of a typical grid used in the calculations. The cells are closely spaced in the radial (r) direction across the shear layer, where the large structures form, and they become farther apart as the distance from the shear layer increases (for $r > D$). The cell separations in the streamwise direction (x) also increase in size moving away from the lip of the nozzle, located at $R = 0.7$ cm and $x = x_o = 0$. The cell sizes are essentially constant in the small dotted-box area of interest in figure 1. In general, Courant numbers in the range 0.4 – 0.5 were used in the calculations. There are 100 – 135 computational cells in the cross-stream (radial) direction and 330 – 410 cells in the streamwise (axial) direction. The mesh spacings vary in the ranges $0.05 \leq \Delta x \leq 0.52$ cm and $0.02 \leq \Delta r \leq 0.67$ cm for the coarser grids, and in the ranges $0.03 \leq \Delta x \leq 0.29$ cm and $0.01 \leq \Delta r \leq 0.67$ cm for the finer grids.

In the case of initially laminar free jet flows with very large Reynolds numbers, shear stresses and dissipation terms are significant only in the very thin layers of the flow on the surface of the nozzle and across the shear layer. The nozzle boundary layers are important in determining the flow near the edge of the nozzle and the initial thickness of the shear layer. The latter thickness and the jet diameter provide the two lengthscales for describing the circular jet flow in the initial region; sufficiently farther downstream, the diameter becomes the only lengthscale. In the free shear flow sufficiently downstream of the nozzle, the large-scale coherent structures should be essentially independent of Reynolds number.

The boundary layers in the nozzle have not been explicitly included in our calculations. To determine an effective initial momentum thickness θ_o of the shear layer we note that the Strouhal number, $St_{\theta_o} = f\theta_o/U_o$, associated with the natural instability frequency of the shear layer, lies in the range 0.0125 – 0.0155 (Husain & Hussain 1983). Based on the spectra of axial velocity fluctuations (see section 3.1 below) we can obtain a characteristic value $St_{\theta_o} = 0.014$ in this range. If the initial momentum thickness of the shear layer θ_o is chosen to be effectively equal to the thickness of the rim of the nozzle in the simulations, that is, one cell length across the shear layer.

For easy reference this value of θ_o will be used as the lengthscale of the shear layer. In order to see that this is consistent, we can use a typical longitudinal phase velocity, $u_p = f\lambda_o \approx 0.6 U_o$, to estimate $\theta_o/\lambda_o \approx St/0.6$. Thus, for St in the range $0.0125 - 0.0155$, one wavelength (λ_o) of the natural oscillation of the shear layer downstream of the nozzle exit is resolved with $39 - 48$ cells in the transverse direction and $16 - 19$ in the streamwise direction. Therefore, the spatial details of the large-scale structures and their spatial evolution are well resolved. Moreover, we show below that there is good agreement between the calculated and experimental results when this choice of θ_o is used as an effective lengthscale of the shear layer in the simulations.

3. RESULTS AND DISCUSSION

The plan of this section is as follows. In Section 3.1 we investigate the instantaneous large-scale spatial features of the flow with special emphasis on the correspondence between the vorticity and pressure fields. Then, in Section 3.2 we study the time-averaged quantities to examine the effect of the initial conditions on the jet flow. Compressibility effects are assessed in Section 3.3. Coherent-structure dynamics are studied in Section 3.4 in order to understand specific observed features of the flow. The streamwise momentum flux of the jet is studied in Section 3.5 for the case of unforced jets as a function of the initial shear-layer thickness and Mach number. Finally, the effect of controlled excitation at the jet inlet is briefly examined in Section 3.6. The sum of the results presented provides a detailed picture of the correspondence between the increases in streamwise momentum flux and the formation and interaction of coherent structures in the axisymmetric jet.

3.1 Instantaneous Flow Visualization

We focus here on results for the case of a Mach 0.57 jet with $U_o = 2 \times 10^4$ cm/s, and θ_o in the range 0.01 − 0.02 cm. Figure 3 shows typical instantaneous contours for $\theta_o = 0.02$ cm (i.e., $D/\theta_o = 70$) of the azimuthal vorticity, static pressure, and velocities, in the plane of symmetry of the jet. Local minima of the static pressure occur at an essentially fixed distance $x_1 \approx 1D$, where the vorticity sheet rolls up. The vortices move downstream, interact with each other, and thereby spread the vorticity until the central, potential core of the jet disappears at x_*, approximately between $4D$ and $5D$ (consistent with laboratory observations). The observed quasi-periodic flow pattern is characteristic of axisymmetric jets. As a result of their mutual interaction, the vortex rings merge at nearly fixed locations, $x_2 \approx 2D$, $x_3 \approx 4D$, where the centers of the vortex-ring cores are aligned in the radial direction and where the amplitudes of the corresponding subharmonics saturate (Zaman & Hussain 1977; Ho & Huang 1982). The first radial displacement of the vortex rings is used for our definition of the merging locations. We have not observed the vortex rings to roll around each other more than once before their merging. Thus, this gives a consistent definition of the merging locations – given somewhat upstream of the locations where the merging structures become indistinct and the mergings are actually completed. The vortex interactions are promoted by small displacements of the newly formed structures from the center of the shear layer as they are convected downstream. These displacements are likely to be caused directly or indirectly by pressure and velocity fluctuations originated by perturbations downstream at vortex-ring mergings and at the end of the potential core. The vortex rings are either slowed down or accelerated in their convection downstream, depending on whether they are shifted away or towards the centerline of the jet by the radial displacements. When the displacements are properly phased with a pair of structures sufficiently close to each other, the structures roll around each other by mutual induction, which leads in turn to the vortex merging.

Vortex-ring merging appears to be the mechanism for the spread of the shear layer in the present simulations. Spreading due to viscous diffusion is expected to be much less important in the limit of high Reynolds number, and is negligible here due to the very small residual numerical viscosity of our inviscid numerical model. Other mechanisms of shear-layer spreading such as continual fractional, partial and total pairings as well as vortex tearings (Hussain & Clark 1981), were not observed in this simulation. In this paper we concentrate on the transition region of the jet upstream of the end of the potential core, where the flow dynamics can be expected to be captured realistically by the simulation. Three-dimensional effects not considered in the simulations are definitely important near the end of the potential core, so that any discussions of two-dimensional structures beyond this point is of questionable relevance to the physical situation. However, such two-dimensional simulations are useful for comparison with future three-dimensional simulations in order to assess the role of three-dimensionality and to understand the differences between the flow physics in the different dimensionalities.

Figure 3b shows that in the transition region of the jet, the pressure drops about 11%, 14%, and 22% below ambient at the locations of vortex roll-up x_1, and vortex merging at x_2 and x_3, respectively. Such minima are associated with centers of passing vortical structures. The pressure rises above ambient between the structures because of the occurrence of stagnation points there in the reference frame of the advected structures. Positive pressure changes of up to 8% are calculated. The pressure distribution in space is a direct consequence of the instantaneous large-scale coherent *structures in the flow. The correspondence between instantaneous pressure and vorticity field* can be clearly discerned in numerical simulations but is considerably more difficult to establish experimentally. The pressure increases are discussed in detail in the later sections.

The spectra of the axial velocity fluctuations at $r = 0$, the center of the jet, and $r = D/2$, the initial center of the shear layer, are shown in figure 4 at selected streamwise locations. The spectra are based on time series which exclude the initial flow transient and have a time-duration of 28–56 vortex roll-up periods. Just downstream of the nozzle lip ($x = 0.5D, D$ and $r = D/2$), the spectra shows a dominant frequency peak at $St_{\theta_o} \approx 0.014$ associated with the vortex-sheet roll-up process. The spectral amplitudes corresponding to the first two subharmonics of St_{θ_o} grow as we move downstream and attain their maximum values at $x \approx 2D$ and $x \approx 4D$, the first and second merging locations, respectively. A similar streamwise evolution of the spectrum is observed at the centerline of the jet, $r = 0$. As noted previously (Grinstein et al. 1987), the presence near the exit of the nozzle of the spectral peaks corresponding to the subharmonics indicates feedback from the downstream events on to the inflowing jet. The roll-up frequency $St_{\theta_o} \approx 0.014$ corresponds to the natural instability frequency of the shear layer and is within the expected range 0.0125 – 0.0155 (Husain and Hussain 1983). Note that experimental values of St_{θ_o} (Zaman & Hussain 1977)

are consistently lower than the theoretically predicted most unstable value of 0.017, the difference attributed to feedback effects from the structures downstream (Hussain et al. 1986).

Figure 5 shows vorticity contours in a plane passing through the jet axis for the simulation with $\theta_o = 0.01$ cm ($D/\theta_0 = 140$), one half the value of θ_o in the case of figure 3. Decreasing the shear-layer thickness reduces the wavelength of the initial instability and hence the lengthscale of the vortex rings, which allows a third merging to occur before the end of the potential core. Defining x_{i+1} ($i \geq 1$) as the quasi-stable location of the ith-merging, we note that $(x_3 - x_2) \approx x_2$ for both jets. Moreover, $(x_4 - x_3)$ is of the order of $2 - 3$ times $(x_3 - x_2)$. This spacing was seen in previous simulations of two-dimensional axisymmetric jets (Grinstein et al. 1987) and is in agreement with experimental results obtained for weakly excited circular jets (Zaman & Hussain 1977; Kibens 1979). It is also in good agreement with the predictions of a feedback formula suggested by Laufer & Monkewitz (1980) and by Ho & Huang (1982), that describes the feedback between the convection of instabilities downstream and the upstream propagation of acoustic fluctuations. The upstream feedback appears to be responsible for the underlying degree of organization in the axisymmetric free shear layer (see also Hussain & Zaman 1978).

3.2 Time-Averaged Data

Time-average results are presented here for the unexcited jet. Although these results do not capture the dynamics of the coherent structures, they do show the effect of the localization of the roll-up and merging processes on the average properties of the flow. Moreover, these results will also be used as a reference to evaluate the effect of compressibility and controlled excitation on the jet.

The time average $\overline{Q}$ of the quantity Q is calculated based on

$$\overline{Q} = \lim_{T \to \infty} \frac{1}{T} \int_0^T Q(t)dt, \tag{6}$$

where the integration interval is chosen in such a way that excludes the initial flow transient, and in practice we use a finite time T – typically in the range of 32–72 vortex roll-up periods – which is adequate to show the outstanding statistical features of the results.

In figure 6 the normalized width of the shear layer, B/θ_o, is shown as a function of x/θ_o. Here, $B = (R_{0.08} - R_{0.92})$, where R_k is defined for a given x as the radial location at which $\overline{u} = U = kU_o$. The figure shows the approximately linear growth of the mixing layer in the axial direction for both calculated and experimental results, and the good agreement among the growth rates dB/dx. The experimental data for initially turbulent free air circular jets corresponds to the case with lowest

inflow fluctuation level studied by Hussain & Zedan (1978), and to the experiments of Husain (1981). In the simulations, the growth rate of the mixing layers decreases immediately downstream of the locations of quasi-stable vortex roll-up and vortex merging indicated by the arrows in the figure. The relative locations of the mergings depend on the wavelength of the most amplified mode. For $\theta_o/D \ll 1$, as we have here, the properties of the axisymmetric shear layer in the near field of the jet should aproach those of the plane mixing layer. Following the predictions of linear stability theory (Michalke, 1965), this wavelength should then scale with θ_o for a given jet velocity. In agreement with this theory figure 6 shows that the distances from the nozzle edge to the vortex-ring roll-up and merging locations scale with θ_o. Figure 7 shows similar variations of the axial RMS velocity fluctuations u'/U_o along the centerline of the jet as a function of the ratio D/θ_o, indicating also that the fluctuation level at each streamwise location x/θ_o roughly scales with θ_o/D.

Figures 8a-e show contours of the time-averaged streamwise velocity U/U_o, Reynolds stress $\overline{\rho u v}/(\rho_{amb} U_o^2)$, RMS axial velocity fluctuations $u'/U_o = (\overline{u^2})^{\frac{1}{2}}/U_o$, static pressure $(\overline{P} - P_{amb})/P_{amb}$, and RMS cross-stream velocity fluctuations $v'/U_o = (\overline{v^2})^{\frac{1}{2}}/U_o$, where $u = \mathrm{u} - U$ and $v = \mathrm{v} - V$ are the instantaneous velocity fluctuations. Figure 8a again shows the approximately linear spread of the shear layer, with the maximum spread rate of the flow occurring near the locations of the maxima of $\overline{\rho u v}/(\rho_{amb} U_o^2)$ (in figure 8b) and those of u'/U_o at the center of the shear layer (in figure 8c), somewhat upstream of the corresponding locations of vortex roll-up and vortex merging at the maxima of v'/U_o. The spread rate decreases downstream of the third maximum of $\overline{\rho u v}/(\rho_{amb} U_o^2)$, for $x > 2D$. This region of reduced growth rate is associated with a region of negative Reynolds stress (discussed further below in Section 3.4).

Figure 8d shows that the mean static pressure varies within 3% of ambient pressure; it is generally below ambient in the mixing layers and above ambient in the potential core of the jet. The locations of local pressure minima coincide with the maxima of v'/U_o in figure 8e, that occur in the neighborhood of the locations of vortex roll-up and vortex merging. This indicates the crucial role of the large scale features of the coherent structures whose imprint is manifest in both the cross-stream velocity fluctuations increases and the static pressure decreases within the shear layer. In addition, we note that the pressure maximum just downstream of the second merging location (also discussed below in 3.4) appears clearly associated with a region of larger u'/U_o near the centerline of the jet at $x \approx 2.3D$ in figure 8c, and at $x \approx 320\theta_o$ in figure 7, in the neighborhood of the second merging location.

3.3 Effects of Compressibility

In order to assess the effects of compressibility on the flow, we have studied the case of a lower Mach number ($M = 0.43$) unforced free jet with the same diameter and ratio $D/\theta_o = 140$, and with

$U_o = 1.5 \times 10^4$ cm/s. Figure 9 shows a typical instantaneous flow visualization for this case. For a given effective initial thickness of the shear layer, the effect of decreasing the jet velocity is to increase the smallest characteristic lengthscale of the jet, namely the lengthscale of the structures that roll up with the natural shear-layer instability mode. This is expected because the size and spacing of the rolled up structures scale on θ_o and U_o; (in a given experimental facility U_o and θ_o are uniquely related).

Because of the larger structures involved in the flow, the spread rate of the shear layer due to vortex-ring roll-up and vortex-ring pairings is higher for the slower jet (see figure 10) and the potential core becomes shorter. In contrast to the higher Mach number case discussed above, for the same ratio D/θ_o, where up to the third merging occurred before reaching the end of the potential core, only the first and second vortex-ring pairings now occur (cf. figures 5 and 9). Figure 11 shows contours of mean static pressure for this jet. The pressure changes are also relatively smaller than in the $M = 0.57$ case, consistent with the decreased magnitude of the vorticity (which scales with U_o), when $M = 0.47$. The peak values of negative pressure within the shear layer region and of positive pressure within the potential core drop about 30% and 50%, respectively. Because the ratio of negative to positive peak pressure is larger in this case, the pressure-drops in the shear layer now become relatively more important than the increases within the potential core. This is consistent with the faster spread of the mixing layer and results in a faster increase in the streamwise momentum flux for lower Mach number (discussed below in Section 3.6).

3.4 Coherent Structures

In this section we examine the detailed coherent-structure dynamics of the flow in order to understand the origin of the region of negative Reynolds stress $\overline{\rho u v}/(\rho_{amb}U_o^2)$ in figure 8b and of the mean pressure maximum in figure 8c. We first examine a sequence of contours of instantaneous vorticity and Reynolds stress $\rho u v/(\rho_{amb}U_o^2)$ in figures 12 and 13. The sequence shows some of the details of two fairly complete cycles associated with the first and second mergings. The *tilt* of a vorticity distribution with an elliptically shaped cross-section can be defined in terms of the alignment of its major axis with the direction of strain rate. Likewise, the orientation of the line connecting the centers of the vortices involved in a pairing process can be used to define the tilt of the associated elliptically shaped vorticity distribution. The downstream (positive) tilt of the line connecting two pairing vortices (i.e., slope opposite to that of the velocity profile) shows that there is a preferred momentum transport from the jet towards the shear layer which will have the effect of increasing the turbulent kinetic energy. When the tilt is negative, i.e., when the line connecting vortex centers is aligned with the mean velocity gradient, the momentum flux is away from the mixing layer, and hence the turbulent kinetic energy decreases (Browand & Ho 1983; Hussain 1983; Ho & Huerre 1984; Zaman & Hussain 1977). Figure 13 indicates that positive

Reynolds stress (solid-line contours) predominates at the stage of the pairing in which the tilt is positive. Past the stage when the vortices are aligned vertically, which defines the pairing location (provided that the vortex rings roll around each other only once before merging), the tilt becomes negative, and negative Reynolds stress (dashed contours) increasingly predominates in the region of the merging. These properties of the Reynolds stress during the pairing process were previously noted in experimental studies of the mixing layer of a circular jet (Zaman & Hussain 1977) and in temporal simulations of a plane mixing layer by Riley & Metcalfe (1980).

The turbulence production, $\Pi \approx -\overline{uv}\partial U/\partial r$, measures average energy transfer from the mean to the turbulent flow when $-\overline{uv}$ and $\partial U/\partial r$ have the same sign ($\Pi > 0$). Otherwise, counter-gradient momentum transport takes place and the energy is transferred on the average from the turbulent to the mean flow. In general, if succesive pairings occur in the shear layer as we move downstream, the positive tilt predominates in the flow and the growth of the mixing layer ensures that it remains actively turbulent. Thus the regions of negative Π will not be important for the average flow, and will not be observed provided that the growth of the shear layer, and hence the positive tilt, are sustained.

Negative production has been observed in plane mixing layers where the growth of the shear layer has been suppressed by appropriate forcing (Oster & Wygnanski 1982). By localizing succesive mergings in axisymmetric jets, it has also been observed in the region immediately downstream of the pairing location (Zaman & Hussain 1977; Hussain & Zaman 1980). In the present simulations we observe negative time-averaged Reynolds stress in figure 8b, immediately downstream of a vortex merging occurring at $x \approx 2.1D$ in the case of the $\theta_o = 0.01$ cm jet, and further on downstream (at $x \approx 4D$) for the jet with $\theta_o = 0.02$ cm. In this region, the tilt is predominantly negative, and figure 6 indicates that the shear-layer growth slows appreciably. Upstream of that location, the succesive and relatively close occurrence of the initial roll-up and the first and second mergings causes a steady growth of the shear layer with predominately positive tilt, and hence the preferred positive $\overline{puv}/(\rho_{amb}U_o^2)$ in the first two diameters of the jet in figure 8b. However, the third merging only occurs for $x > 4D$ for this jet and this explains the region of reduced growth which, in conjunction with the localization of the second merging, determines the observed negative time-averaged Reynolds stress. Capturing these effects associated with the streamwise growth of the shear layer through succesive vortex mergings is possible because we are simulating the flow dynamics for a shear layer evolving both in space and time.

Figure 14 compares contours of instantaneous vorticity from the present simulations with those of coherent (phase-averaged) vorticity for the axisymmetric jet studied by Hussain & Zaman (1980). The experimental data corresponds to a jet excited at a frequency $St_D = 0.85$, which induced stable periodic mergings at $x = 1.75D$. Stable mergings are induced in the simulations by

the self-excitation of the jet via upstream feedback. The figures show that there is a considerable streamwise extent, immediately downstream of a stable merging location, where further mergings are suppressed and the shear-layer growth is reduced. The corresponding regions of negative production are shown in figure 15. The higher peak values in figure 15a reflect the higher degree of organization in the shear layer due to the excitation.

The origin of the observed pressure maximum on the centerline can be investigated by studying the detailed evolution of the instantaneous vorticity and pressure fields. The sequence of frames in figure 16 shows a cycle of the second merging occurring in this particular jet $(D/\theta_o = 70)$ for x between $3D$ and $5D$. As expected and noted earlier, the pressure drops below ambient pressure in the cores of the vortex rings, and rises above ambient pressure between the rings and within the potential core of the jet. In a reference frame advected with the vortex center, the pressure will have a minimum at the vortex center. Similarly, starting from the vortex center the pressure will increase outwards, becoming maximum at the saddles, which are local stagnation points in the moving frame (see figure 17). The interaction between vortex rings leads to the first and second mergings, at $x \approx 2D$ and $x \approx 4D$, respectively. In particular, the instantaneous difference between local and ambient pressure attains maximum values within a toroidal region just downstream of the first merging location (frame a). As the pairing processes continue, the radius of the high-pressure ring initially at $x \approx 2D$ (in frame a) progressively decreases as it convects downstream, focusing on the centerline of the jet (frame b), at $x \approx 4.2D$ for the jet with $D/\theta_o = 70$ (at $x \approx 3D$ for $D/\theta_o = 140$), just upstream of the streamwise location where the second merging is completed. As shown below in figure 24a, which shows contours of $\overline{P}$ for the jet with $D/\theta_o = 70$, the mean pressure has a region of local maxima in the region surrounding this virtual focal point on the centerline.

Maxima of mean pressure on the centerline have not been reported in laboratory experiments with circular jets. Figure 18 shows results for the case of a circular free air jet with $U_o = 2.0 \times 10^3$ cm/s and $D = 7.6$ cm (Toyoda 1986). The mean pressure decreases monotonically along the centerline from values above to below ambient pressure. This behavior was also reported for planar jets (Miller & Comings 1957,; Hussain & Clark 1977). The observed decrease of the pressure values on the centerline of the jet with decreasing Mach number (cf. figures 8 and 11) suggests that these disparities between numerical simulations and laboratory experiments may in part be due to compressibility effects (the jets in the experiments were much slower and virtually incompressible). Furthermore, we note that azimuthal effects are not accounted for in the present simulations and become more important as we approach the end of the potential core. The possible role of azimuthal effects in further reducing the pressure values within the potential core can not be assessed at present.

3.5 Tests of the Isobaric Jet Flow Hypothesis

The mean streamwise momentum flux can be evaluated from the calculated primitive variables. This is done by first integrating the axial component of the momentum balance equation (eq. 2) in the radial and azimuthal directions (with the boundary condition $V = 0$ for $r \to \infty$), and then time averaging the resulting expression. The result is

$$\int_0^\infty \overline{\rho[U^2 + u^2]} r \, dr + \int_0^\infty \overline{P} r \, dr = \text{constant}. \tag{7}$$

From eq. 7 it follows that if the jet flow is isobaric, the streamwise momentum flux is constant. This constancy was universally assumed for many years, and even used as criterion for acceptance of experimental data. However, from eq. 7 it is also consistent with conservation of momentum to have an increase in the average momentum flux as long as it is balanced by appropriate decreases in the mean static pressure integral. Measurements of such pressure decreases were reported by Miller & Comings (1957), and later on by Bradbury (1965), Sami et al. (1967), and Maestrello & McDaid (1971), although corresponding increases in the streamwise momentum flux were not observed or reported. Variations of the streamwise momentum flux were first reported, in connection with planar-jet experiments, by Hussain & Clark (1977), who found an increase in momentum flux and consistent decreases in the static pressure integral. On the basis of the momentum equation integrated in the cross-stream direction, they argued that negative changes of the mean pressure within the turbulent region are supported by the transverse turbulent fluctuations, that is, $\overline{P}(y) - \overline{P}(\infty) \doteq -\overline{\rho v^2}$, where y is the cross-stream coordinate in the planar-jet geometry, and $P(\infty) = P_{amb}$. This relation between negative pressure changes and velocity fluctuations is apparent in figure 6. Hussain & Clark showed that momentum flux increases were accompanied by decreases in the integrated pressure. However, due to the unquantified effects of high turbulence levels on both velocity and static pressure measured in their experiments, the authors could not check the momentum balance quantitatively. The experiments also showed that the extent of the momentum flux increase depends on the initial conditions.

There is a second inherent constraint on the measurements. Because the hot-wire error due to effects of extremely high turbulence levels, including flow reversal, is unavoidable at the outer edges of the jet, the axisymmetric cross-section tends to make the area integral of momentum (hence momentum flux) diverge unless the integration is truncated or the velocity profile constrained to satisfy $V = 0$ for $r \to \infty$ in an appropriate way. Numerical simulation is a useful tool to investigate this matter. Within the accuracy of the simulation, the integrals of mean and turbulent velocities and static pressure are unaffected by large turbulence levels (unlike experiments) and the integrals can be computed much more precisely.

16

We define the streamwise component of the total average momentum flux $\mathcal{M}_T(x)$, and the pressure integral $\mathcal{P}(x)$, as

$$\mathcal{M}_T(x) = \int_0^\infty \overline{\rho(r,x,t)\left(U(r,x)^2 + u(r,x,t)^2\right)} r\, dr, \qquad (8)$$

$$\mathcal{P}(x) = \int_0^\infty \overline{P(r,x,t)} r\, dr. \qquad (9)$$

and rewrite eq. 7 in terms of these quantities, using the values at the nozzle exit as reference,

$$\frac{\mathcal{M}_T(x) - \mathcal{M}_T(x_o)}{\mathcal{M}_T(x_o)} + \frac{\mathcal{P}(x) - \mathcal{P}(x_o)}{\mathcal{M}_T(x_o)} = 0. \qquad (10)$$

Figure 19 compares the two terms of eq. 10 for the unexcited jet. The momentum flux increases up to 9% relative to its value at the nozzle exit and exactly balances the decrease in the pressure integral. This balance is evidence of the accuracy of the numerical simulation of the velocity and pressure fields. Comparing figures 19 and 3, we see that fast changes in $\mathcal{M}_T(x)$ occur in the neighborhood of $x_1 \approx D, x_2 \approx 2D$, and $x_3 \approx 4D$, locations at which vortex rings are relatively strong and well defined and the static pressure has large-scale local minima. Note that in the case of a less organized flow field where the pairing events are not localized the variations of $\mathcal{M}_T(x)$ can be expected to be monotonic as in the data of Hussain & Clark (1977). More disorganized unexcited jet flows would result if azimuthal effects were included or if the run times (and therefore the averaging times) were much longer.

Figure 20 shows the sensitivity of the ratio $\mathcal{M}_T(x)/\mathcal{M}_T(x_o)$ to changes in the cutoff value r_{max}, used in the numerical evaluation of the integrals in eqs. 8 and 9. The growth of the momentum flux along the first five diameters is essentially independent of r_{max} for $r_{max} > 3D$. The cutoff values used for the radial integrations were chosen in this range. The typical averaging times used to evaluate $\mathcal{M}_T(x)/\mathcal{M}_T(x_o)$ varied in the range of 56–72 roll-up periods. With these averaging times, the the peak values of $\mathcal{M}_T(x)/\mathcal{M}_T(x_o)$ at x_1, x_2, and x_3 were estimated to be converged within 2 – 6%, depending on the streamwise location. The convergence becomes slower as we move downstream, e.g., at x_2 and, x_3, since fewer merging realizations than roll-up realizations are involved in the averaging process for a given averaging time.

Figure 21 compares the calculated streamwise momentum flux for the unexcited flow with the available experimental data. For smaller θ_o, more vorticity is concentrated in the shear layer, where there are correspondingly larger decreases in the mean static pressure. According to eq. 9, the contributions to $\mathcal{P}(x)$ from pressure decreases in the shear layer are weighted more (through the factor r) than the increases within the potential core of the jet. This explains the larger values of $\mathcal{M}_T(x)/\mathcal{M}_T(x_o)$ (up to for 33% larger) in the case with smaller initial thickness θ_o, and for

$U_o = 2 \times 10^4$ cm/s). Moreover, for lower Mach number, the shear layer spreads faster (see Section 3.3) and the momentum flux also increases faster, in agreement with the observed trend in the case of the plane-jet experiments reported by Hussain & Clark (1977). These authors also reported the results for the circular jet based on the experimental data of Crow & Champagne (1971), which do not appear to be consistent with the results of the present simulations. However, we note that in contrast with the case of the plane jet, the accuracy of the velocity measurements in the outer edge of an axisymmetric jet is far more crucial because as $r \to \infty$ the outer part of the jet becomes much larger in area. Consequently, hot-wire data cannot be used reliably to evaluate momentum flux because it suffers from large inaccuracies at the high fluctuation levels typical of the outer edges of jets. Other experimental methods such as laser-Doppler anemometry and particle displacement velocimetry can overcome this aspect, even though they have other inherent inaccuracies.

3.6 Effect of Excitation

In this section we study the sensitivity of the results to the presence of controlled planar excitation at the inlet. Excitation or forcing of shear layers has been extensively used in the investigation of the basic mechanisms of shear flows (e.g., Crow & Champagne 1971; Zaman & Hussain 1977, 1980; Ho & Huang 1982). In the present calculations, the jet was excited at the inflow by imposing a sinusoidal (coherent) perturbation of fixed frequency f_1 and relative amplitude a_1 on the free stream inflow velocity U_o, i.e.,

$$U_o \to U_o[1 + a_1 \sin(2\pi f_1 t)]. \tag{12}$$

which provides a controllable planar excitation of the jet stream at the nozzle exit. This imposed perturbation simulates the forcing introduced acoustically in laboratory experiments by speakers located in settling chambers upstream of the nozzle exit (e.g., Zaman & Hussain 1980). In addition, the type of fluctuations that typically occur in experiments, such as free-stream turbulence and boundary layer fluctuations in the nozzle, were also simulated by introducing random perturbations of the streamwise velocity at the nozzle exit (Grinstein et al. 1987). The fluctuations introduced included lengthscales ranging from the initial shear layer thickness to the jet diameter (see the Appendix). The mean fluctuation level of the streamwise velocity of the unforced jets at the nozzle exit was less than 0.5%. In the absence of controlled coherent planar excitation, the inflow fluctuations affect the degree of localization of the mergings (Grinstein et al. 1987). Differences in the time-averaged results due to inflow fluctuations with this level were very small and essentially undistinguishable from the unforced case. We considered low-level coherent (1% - 2%) excitation of the jet with $\theta_o = 0.02$ cm at the nondimensionalized frequency $St_D = f_1 D/U_o = 0.98$, which corresponds to the the natural shear-layer mode (associated with $St_\theta \approx 0.014$ for this jet, i.e., $D/\theta_o = 70$).

18

The coherent excitation of the jet controls the wavelength of the initial instability by periodically modulating the shear layer thickness at its origin. The associated periodic vorticity perturbation propagates in the shear layer which acts as a waveguide. Excitation controls the lengthscale of the structures that roll up in the near field of the jet and can modify the turbulence intensity level. The variations of the streamwise momentum flux are closely related to variations of the mean static pressure and longitudinal turbulence intensity, and thus depend on the particulars of the excitation. As noted above, there is a correspondence between the maxima in streamwise momentum flux and the minima of mean static pressure. In the excited flows, $\mathcal{M}_T(x)$ increases faster near the nozzle than in the unexcited case. This effect is associated with the larger and more organized roll-up process which is induced nearer to the nozzle at higher frequencies.

Figure 22, shows a sequence of instantaneous contours of vorticity during a time interval equal to four excitation periods. Forcing at the shear-layer instability frequency enhances the organization of the flow. The high-frequency excitation forces the initial vortex-ring roll-up to occur closer to the lip of the nozzle. Likewise, the merging locations have also moved upstream: the first merging occurs at $x \approx 1.3D$, and $1.9D$, and the second merging occurs at $x \approx 3.1D$, as compared to $x \approx 2D$ and $x \approx 4D$, respectively in the unexcited case. The contours of Reynolds stress $\overline{\rho uv}/(\rho_{amb}U_o^2)$ (figure 23) show positive peaks upstream of the locations of vortex roll-up and merging and, as in the unexcited case, a well defined region of negative values about $x \approx 3.6D$, just downstream of the second merging location. The values at the first two positive peaks have increased relative to the unexcited case by about 10% and 60%, respectively. The values near the second merging location have increased by about 90% at the positive peak and considerably more at the negative peak. The negative peak value is small and less accurately defined for the unexcited case.

Comparison of the mean pressure distributions for the excited and unexcited cases shows qualitatively the same patterns, but with more pronounced local minima and maxima in the excited case. The mean static pressure (figure 24) again shows minima in the regions of the merging locations and a relative maximum on the centerline near the the region where the second merging takes place. The pressure at the negative peaks vary by -2.4% and -3.0% relative to ambient pressure, as compared to -1.8% and -2.0%, respectively, in the unexcited case. The peak values of Reynolds stress and mean static pressure are noticeably larger as a consequence of the sharper organization of the roll-up and pairing process caused by the excitation. This is also reflected, in the behavior of the longitudinal turbulence intensity u'/U_o along the centerline shown in figure 25.

The growth of the shear-layer thickness is also faster (figure 25) for the excited jet, although downstream of the merging locations it slows down appreciably. The faster growth of the mixing layer in the excited jet is reflected in the growth of the streamwise momentum flux shown in figure 25c. The streamwise momentum flux has pronounced peaks at the merging locations. The

narrower peaks are a consequence of the better localization of the mergings. The momentum flux now increases up to 14% of its value at the nozzle exit. The larger increase in momentum flux due to excitation is considerably more pronounced in the region of vortex roll-up and first merging.

We thus find that the excitation of the shear-layer mode organizes the jet, enhancing the effect of the smaller scales present in the unexcited flow (shown in figures 23–25). Figure 25b indicates that excitation widens the shear layer and, as a consequence, widens the jet. Moreover, the figure also shows that forcing distorts the nearly linear growth of the shear layer observed in the unexcited case. Excitation of the shear-layer instability mode enhances the organization of the shear layer. In particular, the mergings become more localized, and as a consequence the streamwise momentum flux is increased up to about 50% above the results in the unexcited case. The Reynolds stress increases considerably, particularly near the second merging location, where the observed negative production is now much more important.

4. CONCLUSIONS

We have presented results from finite-difference numerical simulations of the transition region of a subsonic, compressible axisymmetric jet at high Reynolds number. We have studied the sensitivity of the results to changes in Mach number, initial shear-layer thickness, and the presence of low-level controlled velocity perturbations at the jet inlet. We have chosen the excitation frequency associated with one of the characteristic lengthscales of the jet, namely, the shear-layer mode. The following conclusions may be drawn from this work.

Self-excitation of the two-dimensional jet due to upstream feedback induces quasi-periodic mergings at nearly fixed streamwise locations. The turbulence production is predominantly positive when the growth of the shear layer is sustained by the succesive relatively close vortex-ring mergings. As the mergings become more separated, a significant decrease in the growth rate of the shear layer occurs downstream of the merging location with consequent negative turbulent production, indicating that there is energy transfer from the turbulent to the mean flow. As was previously asserted based on experimental observations, the origin of this effect is purely kinematical.

The static pressure varies significantly within a free jet relative to that of the surroundings. These pressure variations are associated with the large-scale coherent structures and their interactions. The static pressure decreases within the shear layers and increases in the potential core. Instantaneous pressure drops of the order of 20% were observed at the locations where the vortex rings merge, in contrast with pressure increases of order 8% elsewhere in the jet. The mean static pressure variations ranged within 2–3%.

The total momentum flux in the transition region of the unexcited jet increases above the jet exit value up to a maximum value in the range 9 − 15%, depending on Mach number and initial conditions. The increases are exactly balanced by decreases in the mean static pressure integral, which is consistent with momentum balance requirements and agrees reasonably well with experimental results. The streamwise *mean* momentum flux decreases downstream from the nozzle along the first few diameters of the jet. This is due to the pressure variations within the potential core of the jet, and particularly to the occurrence of a pressure maximum on the centerline near the location where the second merging is completed. As a consequence, the increases in *total* momentum flux in the transition region of the jet are due to the turbulent contribution. This is not, however, inconsistent with the data of Hussain & Clark (1977) within the first four slit-widths of streamwise extent, where the turbulent contribution was of the order of 60%.

Because this numerical simulation resolves sound waves, it deals with finite sound speeds. This requires that a sound wave travel no more than one computational cell length in one timestep, and thus small timesteps dictated by the Courant condition are used in the calculations. If we try to simulate the relatively slow flows investigated in the experiments, the number of timesteps in a

reasonable calculation is considerably large and the computations become impossibly expensive. Patnaik et al. (1986) have developed an implicit FCT algorithm that can bypass the Courant-condition limitation and extend the use of high-order monotonic algorithms to allow long timesteps in slow flows.

APPENDIX

In previous numerical simulations of axisymmetric jets (Grinstein et al. 1987), we studied the effects of random perturbations in the inflowing jet stream. In experiments, such fluctuation may be caused by free-stream turbulence, primarily due to unavoidable acoustic disturbances upstream of the nozzle exit and in the laboratory and boundary layers in the nozzle. In the calculations, the fluctuations are modeled by replacing the streamwise velocity U_o within the nozzle at the inflow boundary (for $r < R$) with $U_o(1+p)$, where $p = p(r,t)$ is the perturbing term. The term $p = p(r,t)$ is added to the sinusoidal term in eq. 12 when coherent excitation is also present, and is defined by a sine Fourier series in the variable R

$$p(r,t) = \frac{1}{N} \sum_{m=1}^{N} p_m^o \delta_m(t) \sin \left(\frac{2\pi m r}{R} + \phi_m \right) , \qquad (A.1)$$

where $\delta_m(t)$ is a time-dependent amplitude defined by (see figure 26)

$$\delta_m(t) = \begin{cases} 2(t - t_{om})/\delta t_m, & \text{if } t_{om} \leq t \leq t_{om} + \delta t_m/2 \\ 2(t_{om} - t)/\delta t_m + 2, & \text{if } t_{om} + \delta t_m/2 \leq t \leq t_{om} + \delta t_m \\ 0, & \text{otherwise.} \end{cases}$$

Each perturbation term in eq. A.1 varies between zero and a maximum value of no more than a fraction p_m^o/M of the inflow jet velocity. The duration δt_m (20–50 timesteps $\approx 0.05\tau_o - 0.13\ \tau_o$, with $\tau_o = \theta_o/(St_{\theta_o} U_o))$, the maximum amplitude p_m^o, and the phases $\phi_m(0 \leq \phi_m \leq 2\pi)$ of the terms in the Fourier series are randomly generated numbers. Starting at $t = t_{om} = 0$, a set $[\delta t_m, p_m^o, \phi_m]$, is generated for each mode. Each set of random numbers is fixed until $t = t_{om} + \delta t_m$, at which time we reset $t_{om} \rightarrow t_{om} + \delta t_m$ and update the set. The number of terms, N, is chosen to ensure that the perturbation includes wavelengths ranging from the initial shear layer thickness θ_o to the diameter D of the jet, thus including the interval of important length scales of the system.

ACKNOWLEDGMENTS
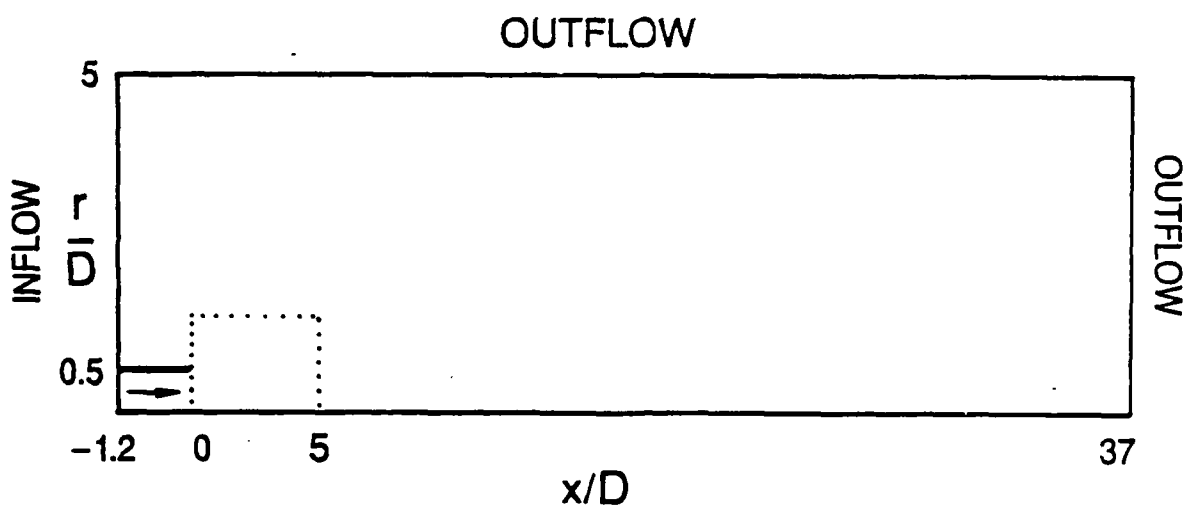
Figure 1

Flow configuration for the simulated axisymmetric free jet.
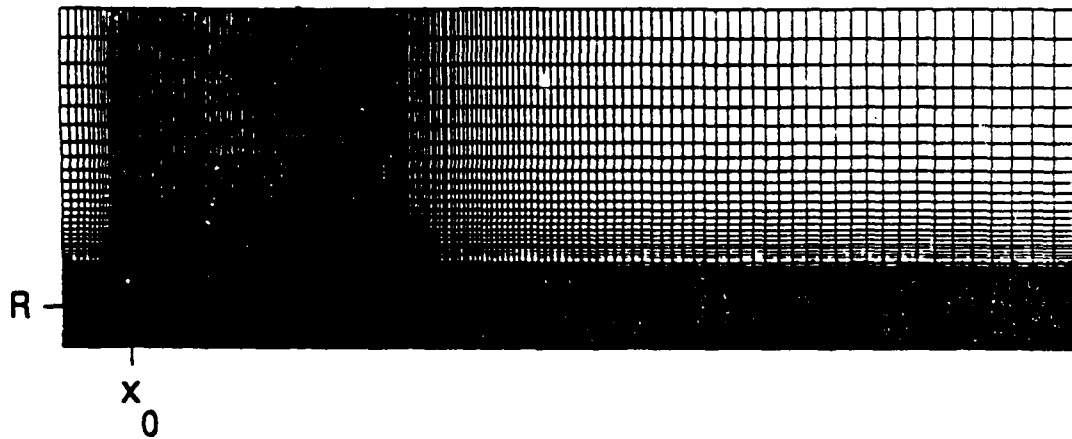
Figure 2

Typical grid used in the simulations.
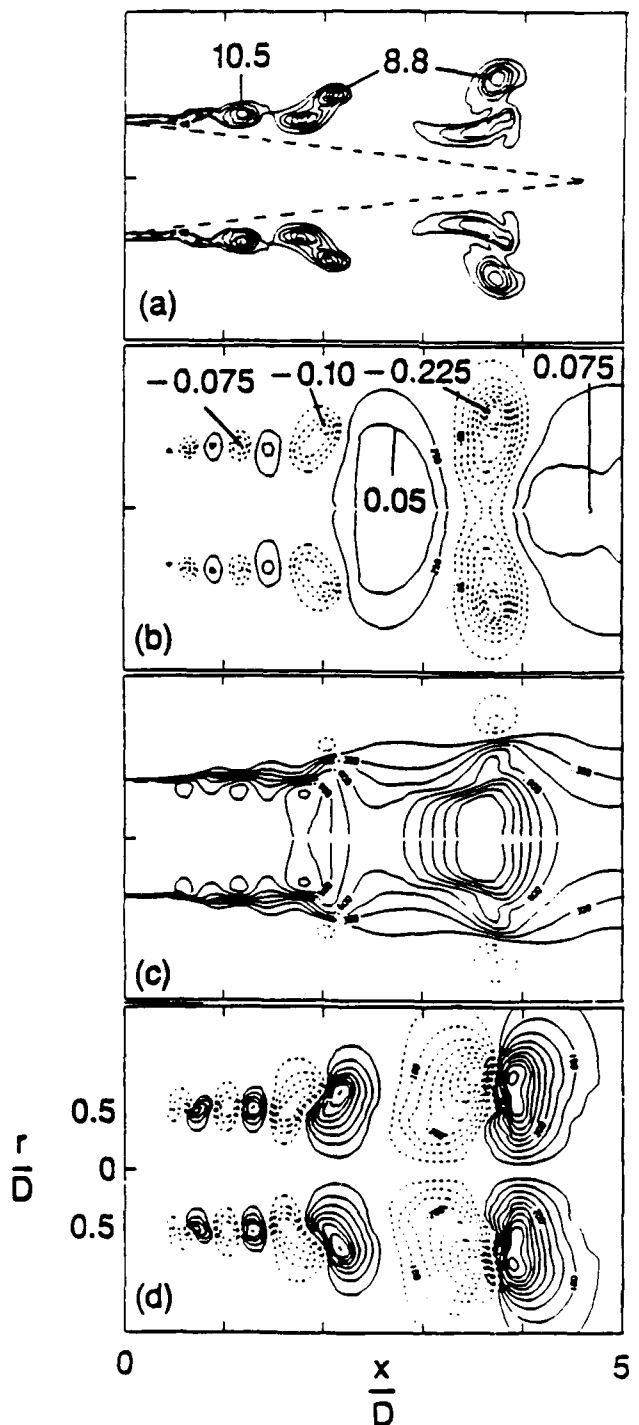
Figure 3

Instantaneous flow visualization for the case $M = 0.57$, $D/\theta_o = 70$. a) Azimuthal vorticity Ω/f_o, with $f_o = St_{\theta_o}U_o/\theta_o$, $St_{\theta_o} = 0.014$; interval between contours, $\Delta=1.8$; b) Relative static-pressure difference $(P - P_{amb})/P_{amb}$, $\Delta=0.025$; c) Axial velocity u/U_o, $\Delta=0.15$; d) Radial velocity v/U_o, $\Delta=0.05$; full : > 0, dashed : < 0;
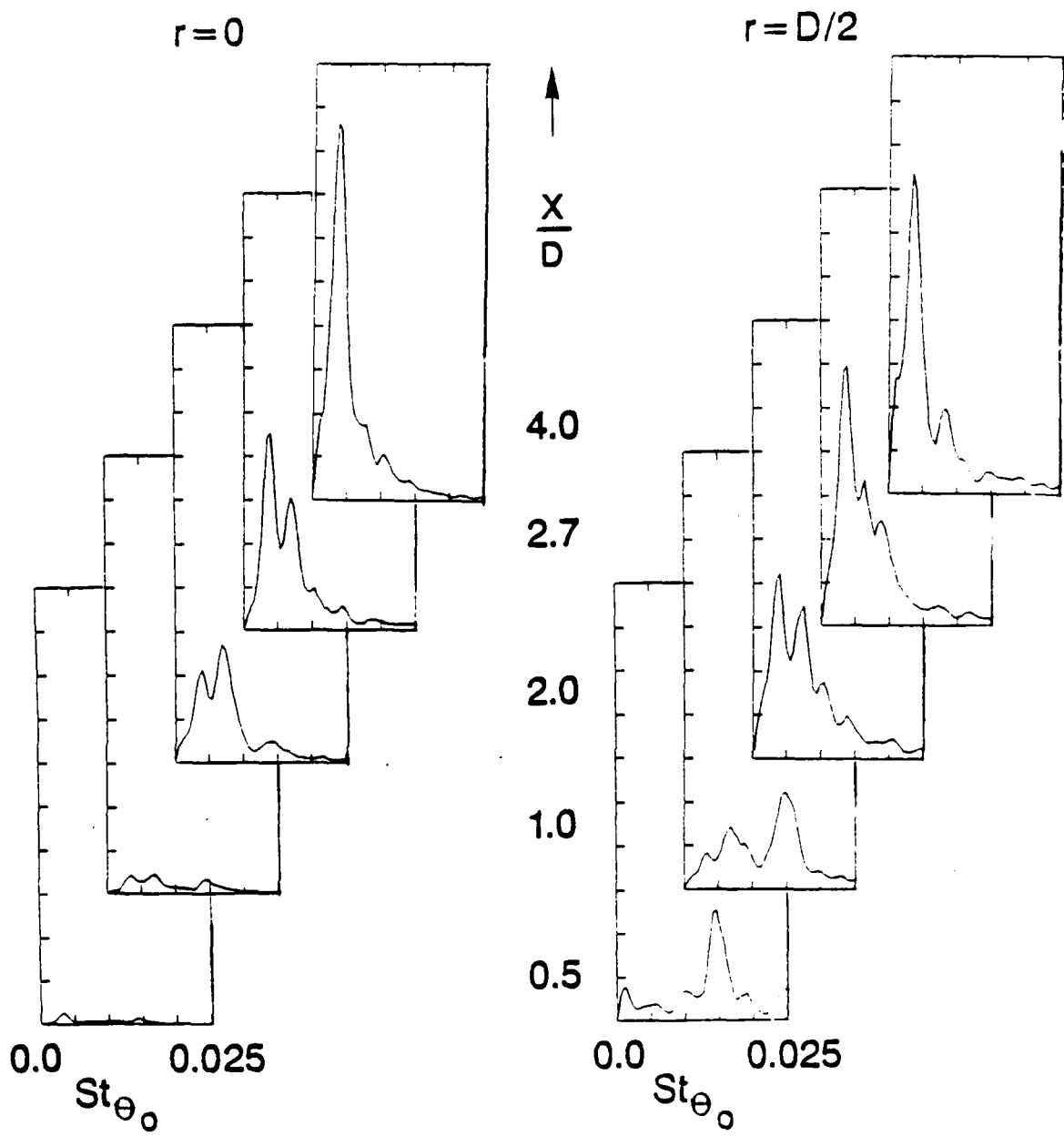
Figure 4

Spectral analysis of the axial velocity fluctuations at $r = 0$, and $r = D/2$ at selected streamwise locations. The vertical scale is linear (arbitrary units).
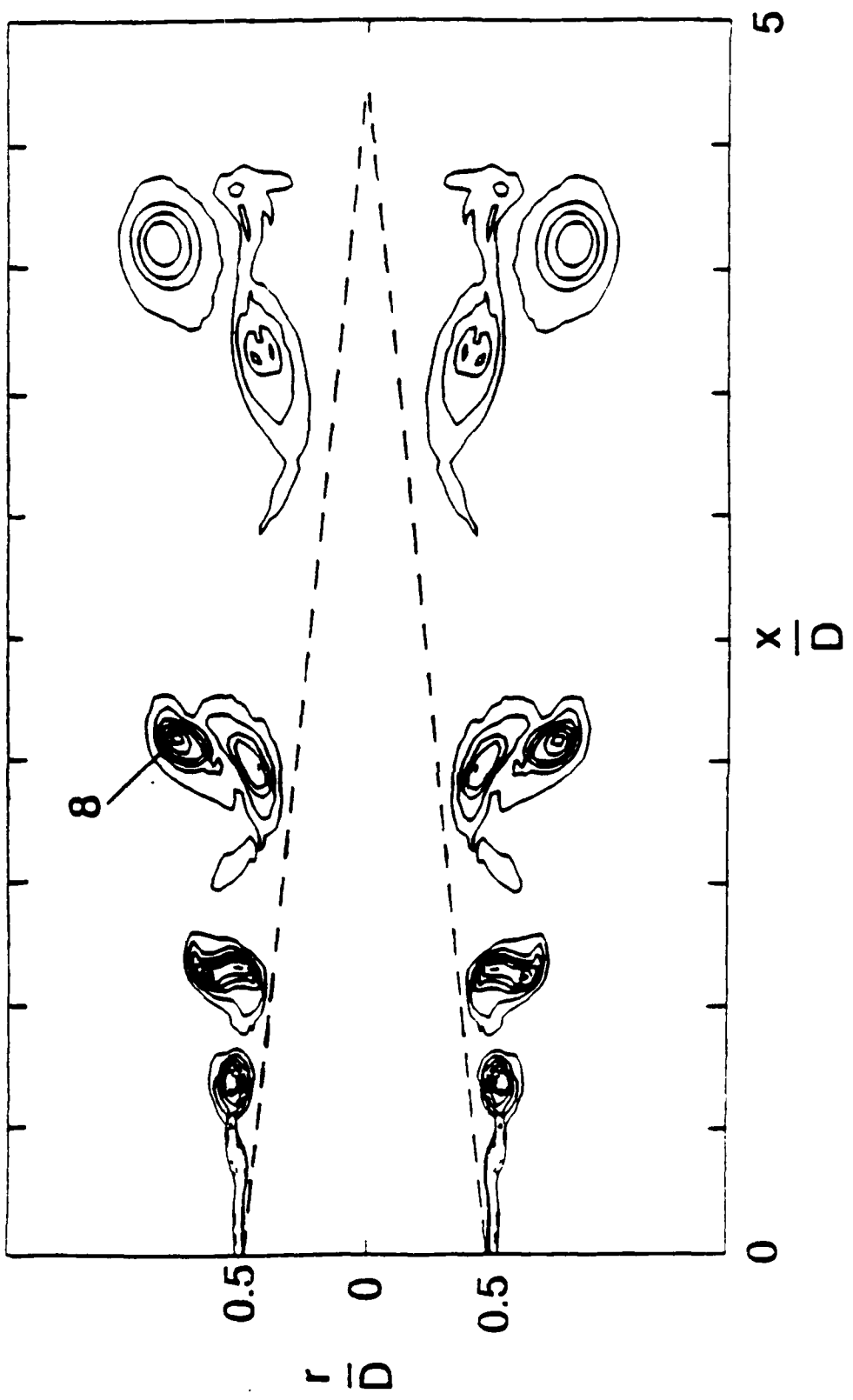
Figure 5

Instantaneous azimuthal vorticity Ω / f_o, for the case $M = 0.57$, $D/\theta_o = 140$; $\Delta = 1.1$.
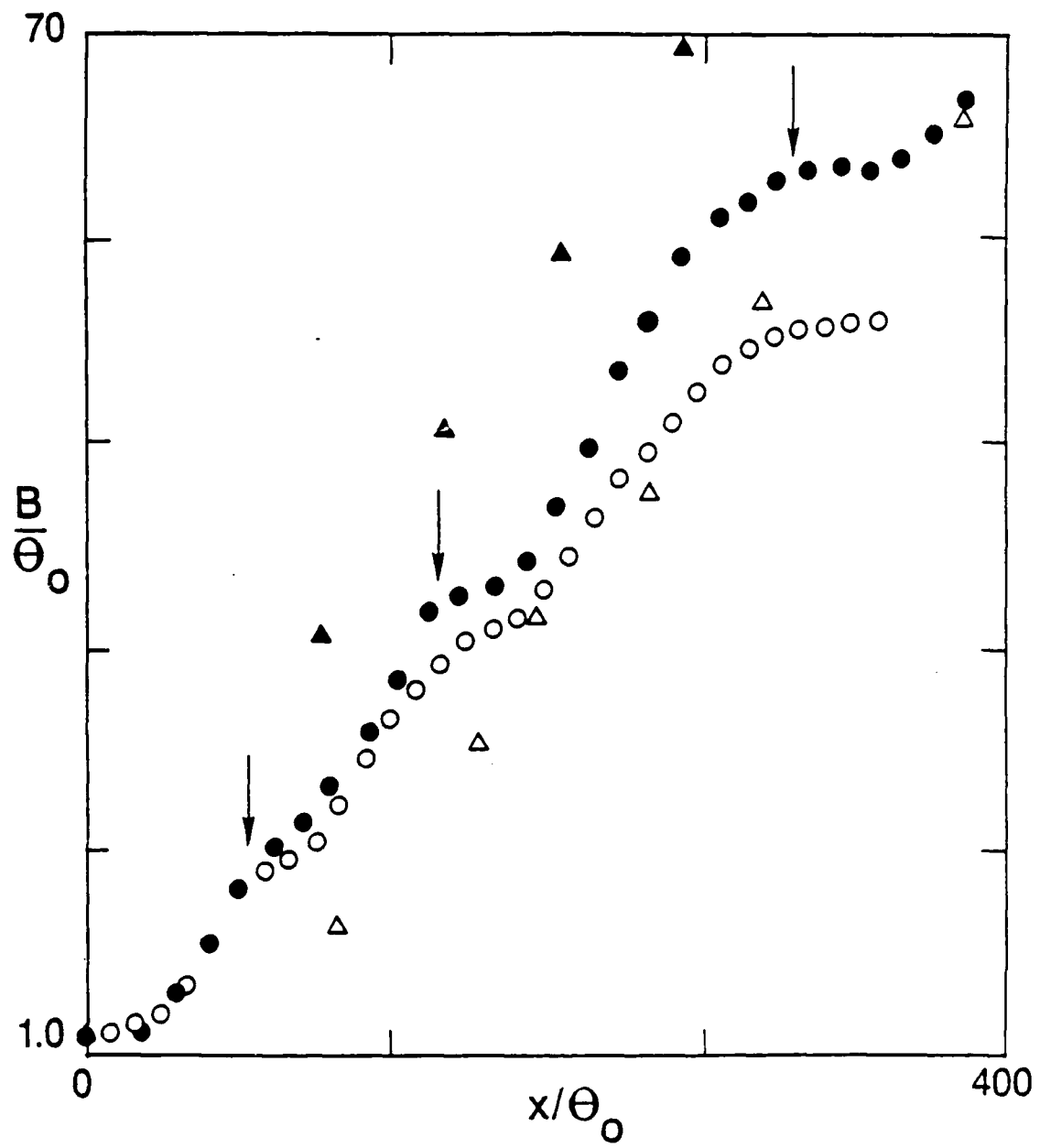
Figure 6

Spread of the mixing layer B/θ_o. ● : $M = 0.57, D/\theta_o = 140$; ○ : $M = 0.57, D/\theta_o = 70$; ▲ : Husain (1981); △ : Hussain and Zedan (1978).
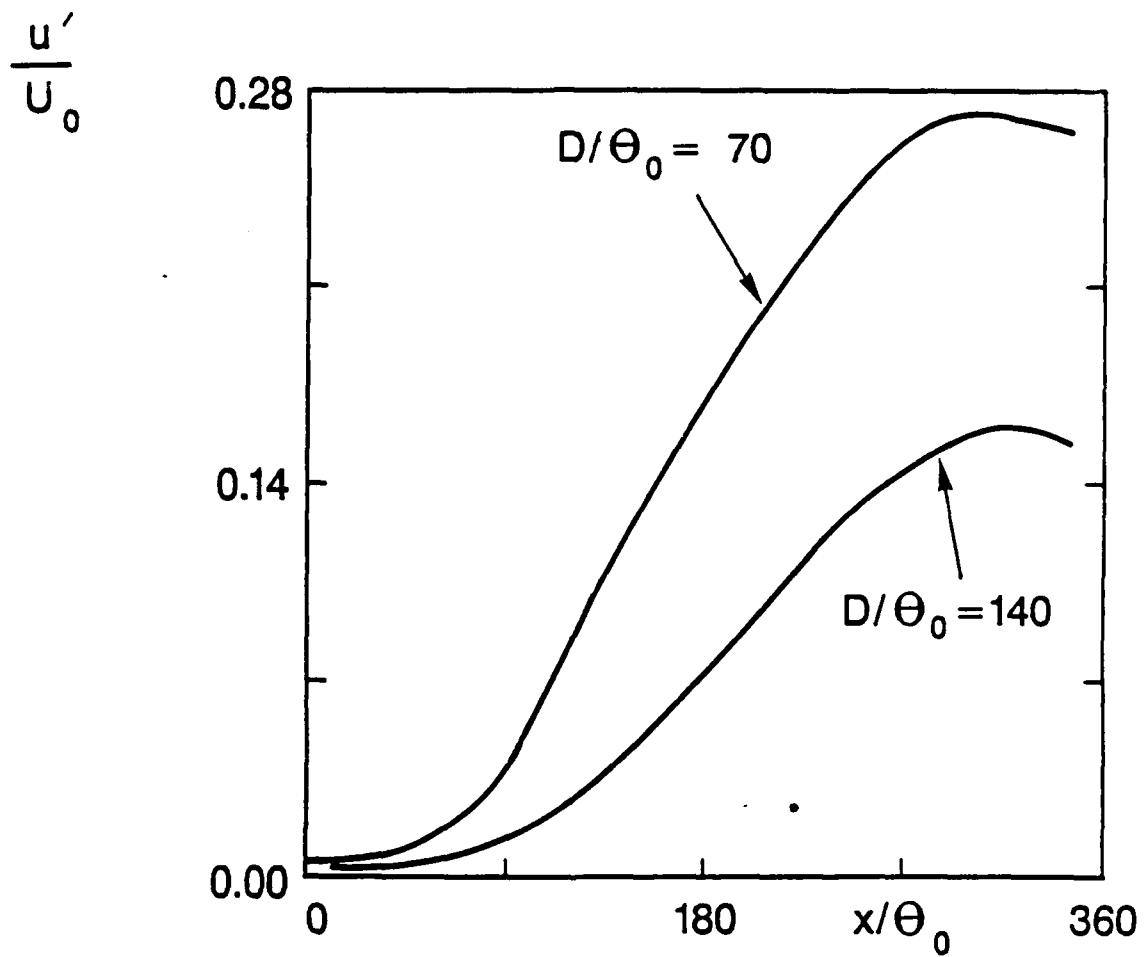
Figure 7

RMS axial velocity fluctuations u'/U_o at the centerline of the jet as a function of the initial shear layer thickness ($M=0.57$).
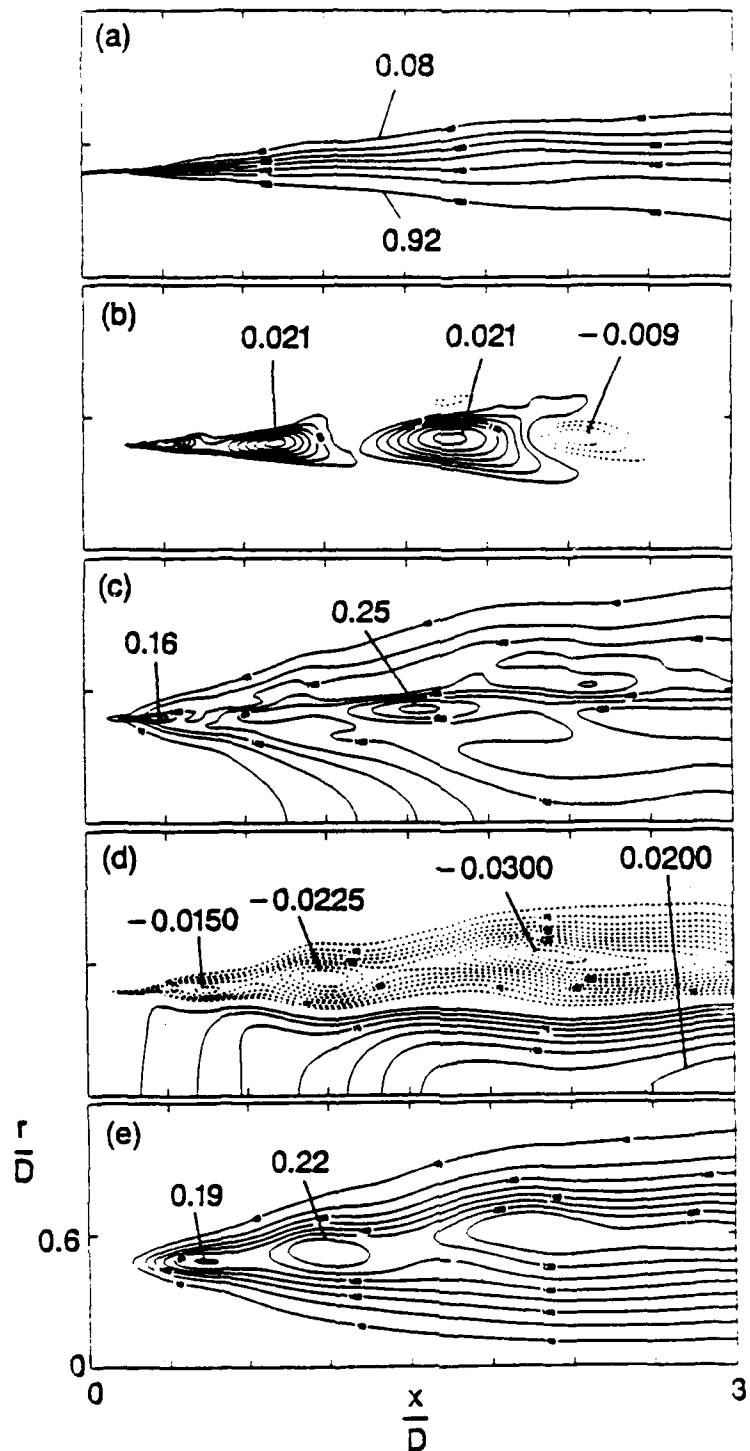
Figure 8

Time-averaged flow results. a) $\overline{U}/U_o$, $\Delta = 0.14$; b) $\overline{\rho uv}/(\rho_{amb}U_o^2)$, $\Delta = 0.003$; c) u'/U_o, $\Delta = 0.3$; d) $(\overline{P} - P_{amb})/P_{amb}$, $\Delta = 0.0025$; full : > 0, dashed : < 0. e) v'/U_o, $\Delta = 0.003$.
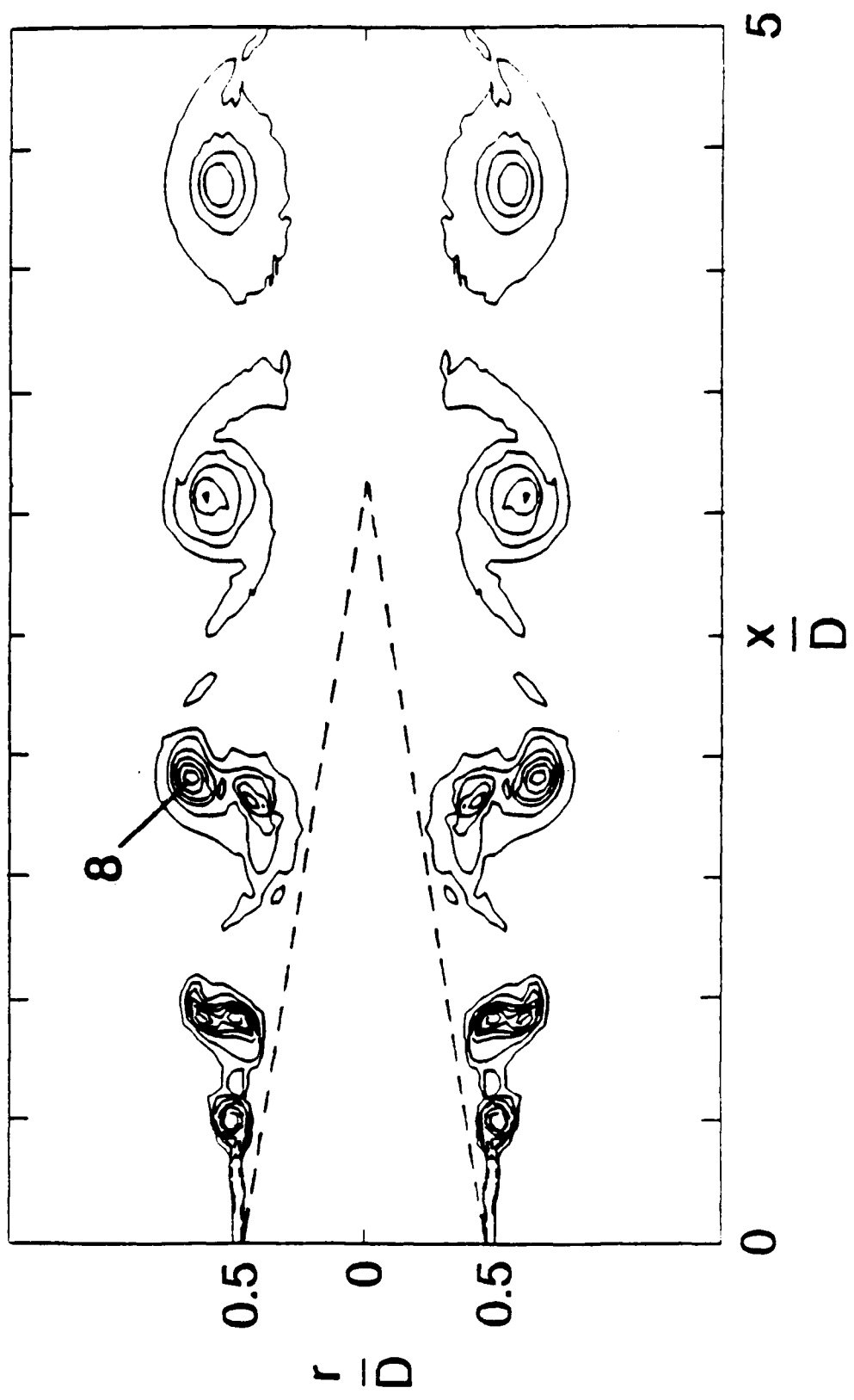
Figure 9

Instantaneous azimuthal vorticity, Ω/f_o, for the case $M = 0.43, D/\theta_o = 140; \Delta = 1.4$
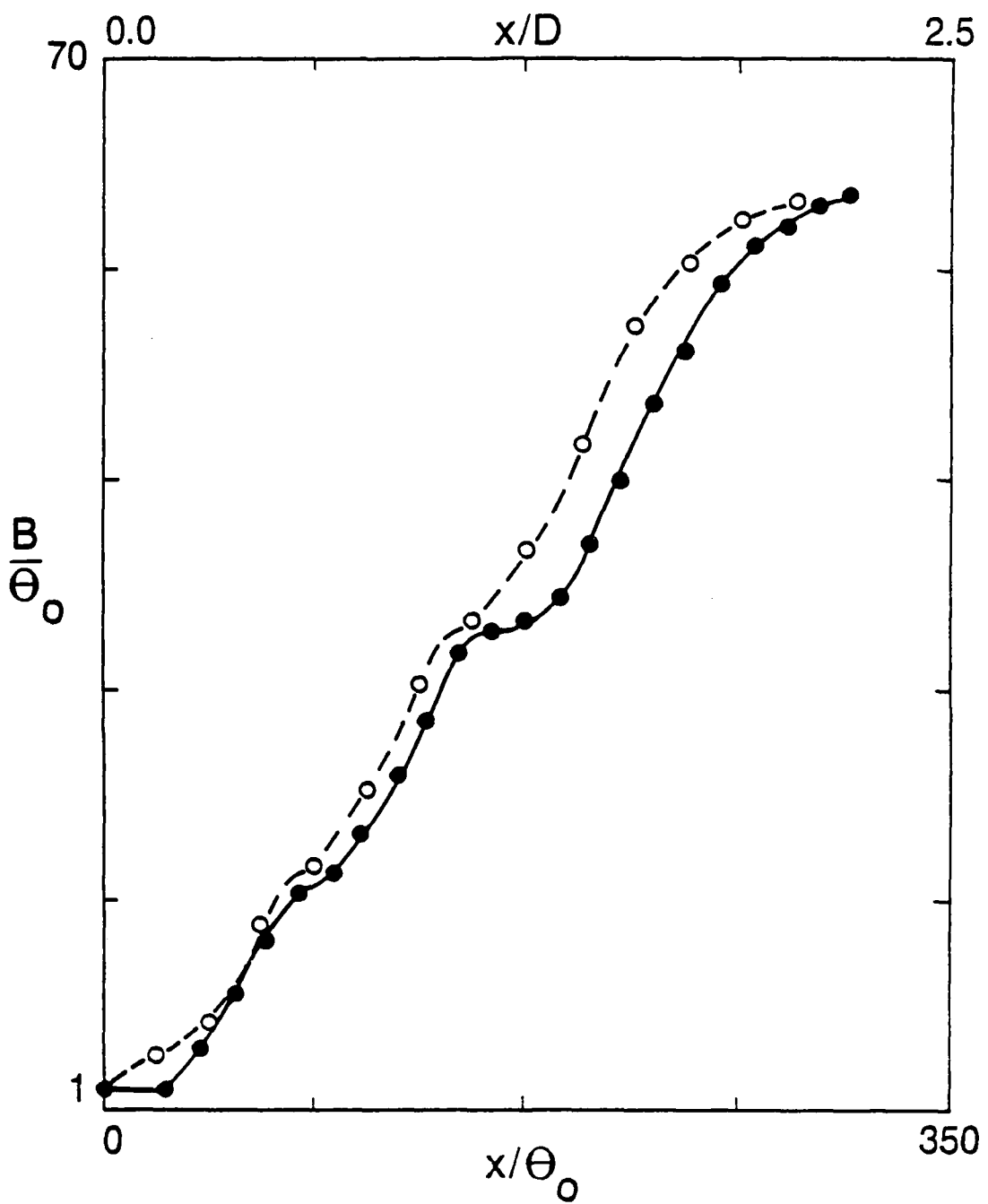
Figure 10

Mixing layer spread vs. M, for $D/\theta_o = 140$; full : $M = 0.57$, dashed : $M = 0.43$.
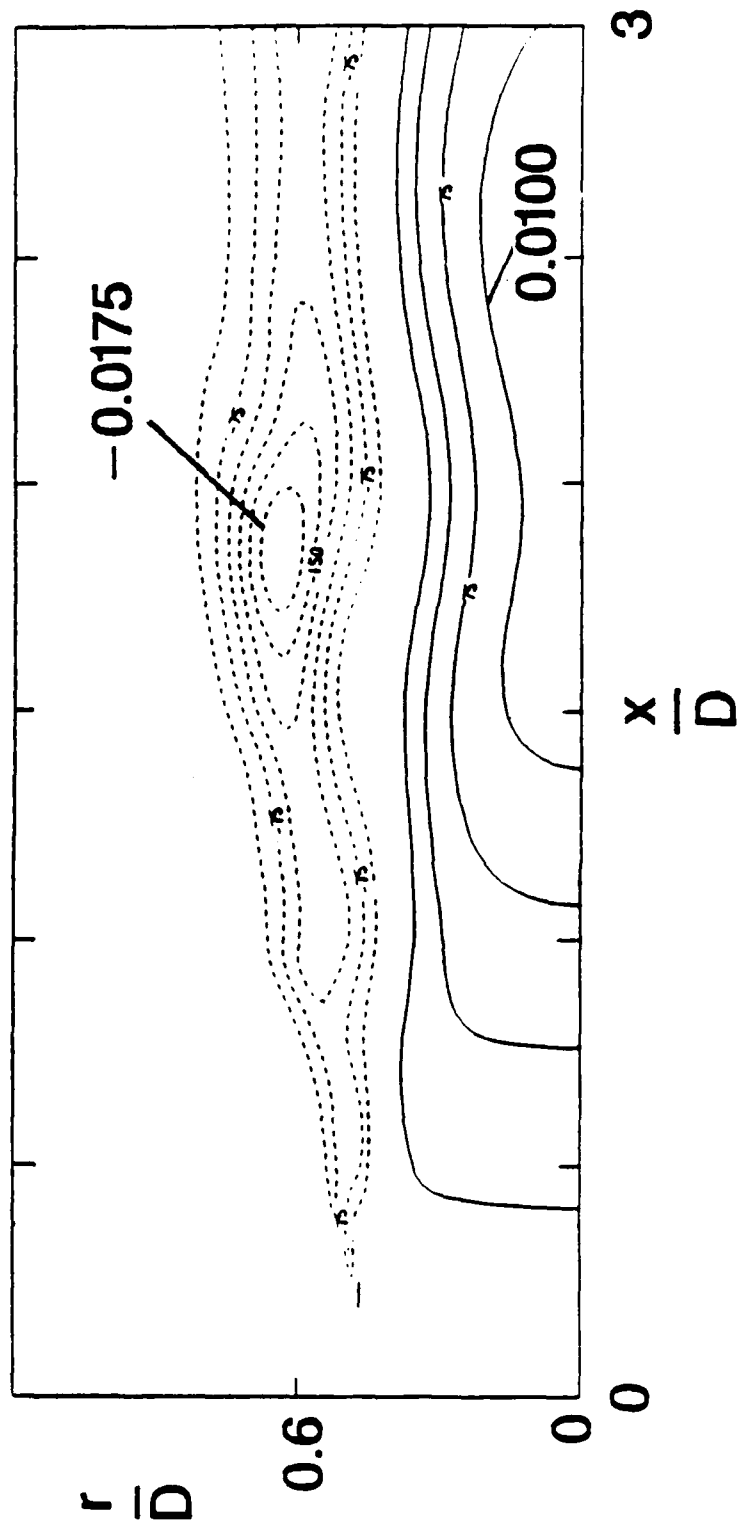
Figure 11

Mean relative static-pressure difference, $(\overline{P} - P_{amb})/P_{amb} \times 10^4$, $\Delta = 0.0025$, for the case

$M = 0.43$, $D/\theta_o = 140$; full : > 0, dashed : < 0.
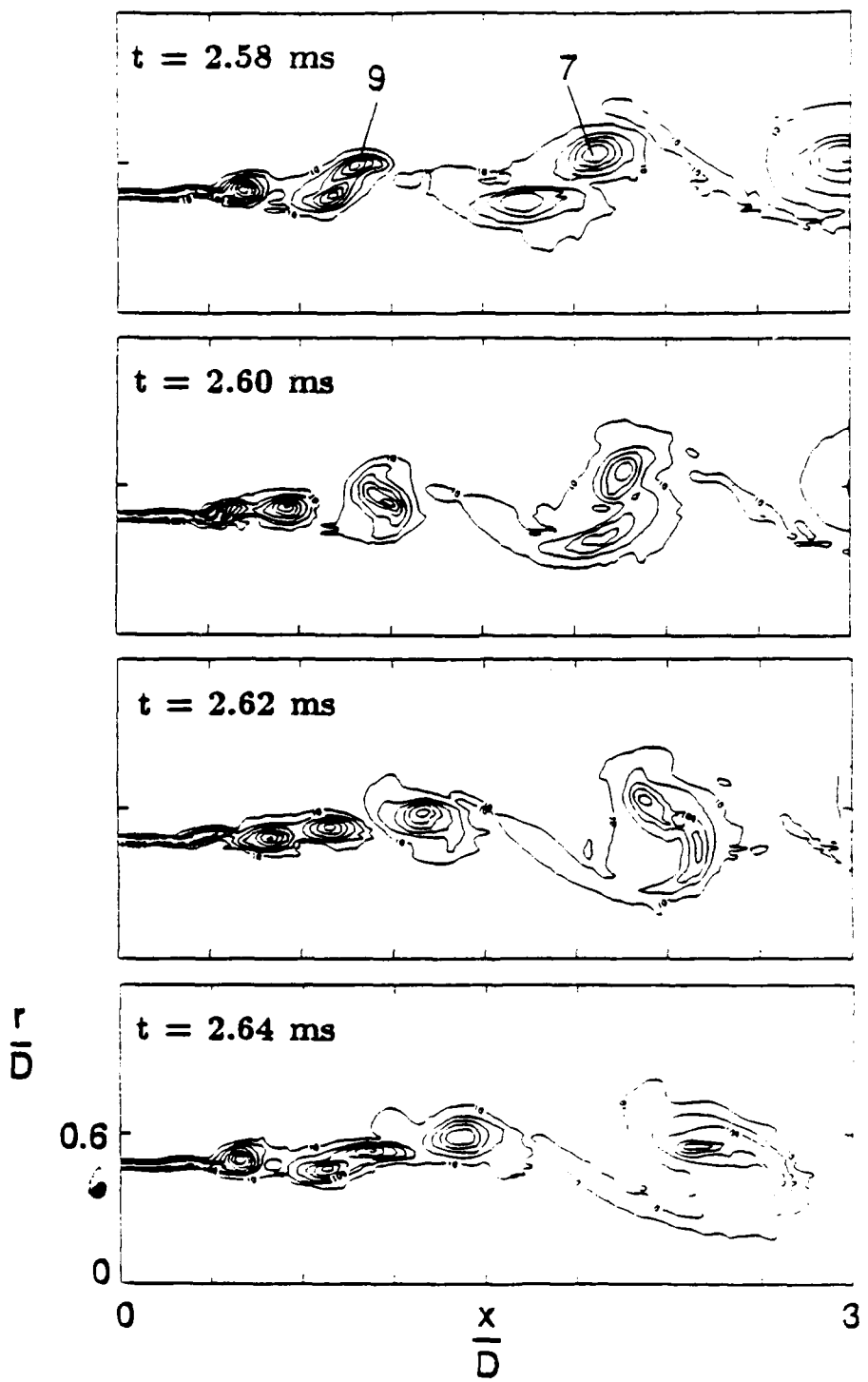
Figure 12

Instantaneous azimuthal vorticity, Ω/f_o, for the case $M = 0.57$, $D/\theta_o = 140$; $\Delta = 1.7$.
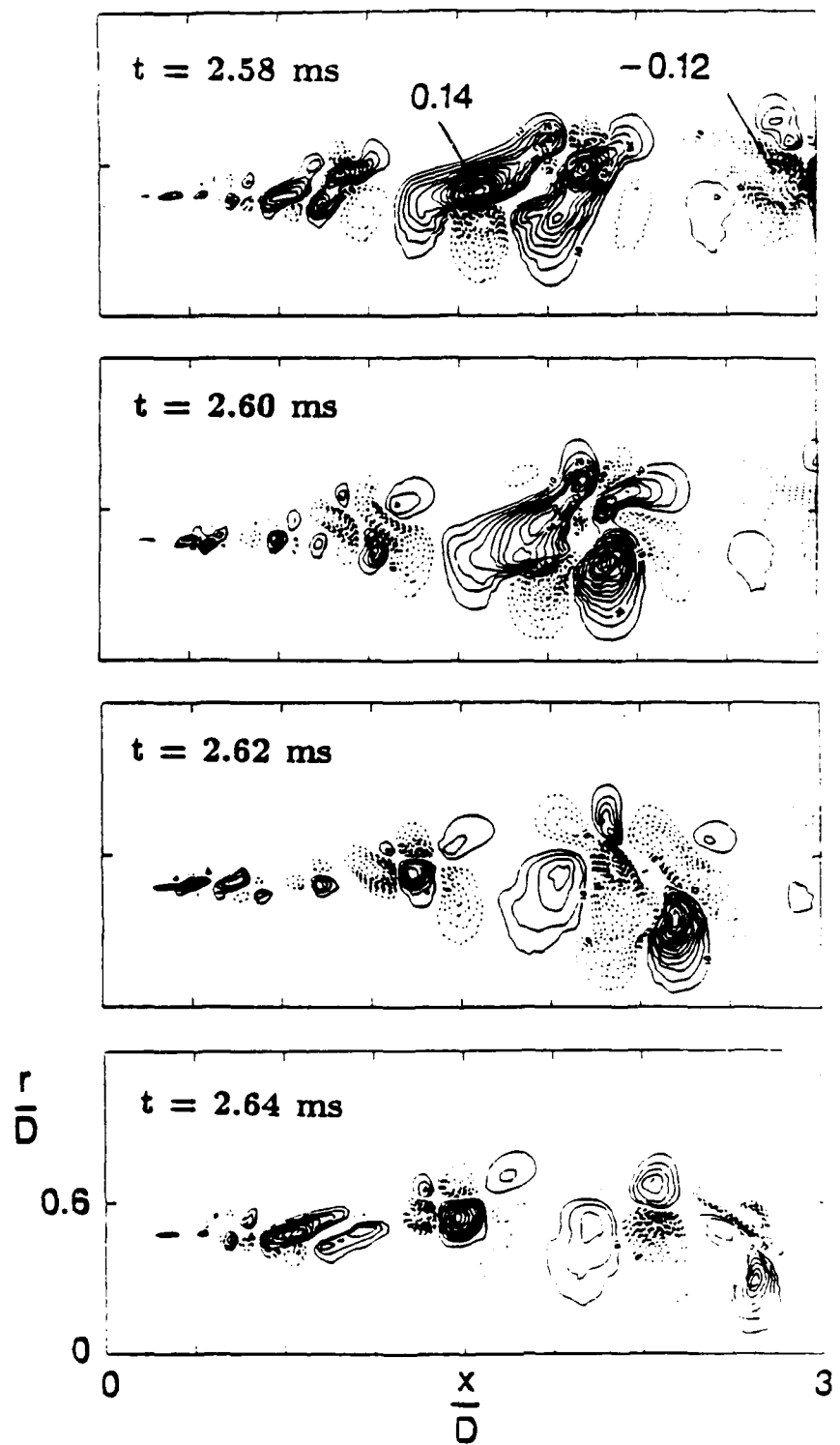
Figure 13

Instantaneous Reynolds Stress. $\rho(u - \bar{u})(v - \bar{v})/(\rho_{amb}U_o^2)$, for the case $M = 0.57$, $D/\theta_o =$
140; $\Delta = 0.00815$, full line: > 0, dashed line: < 0.
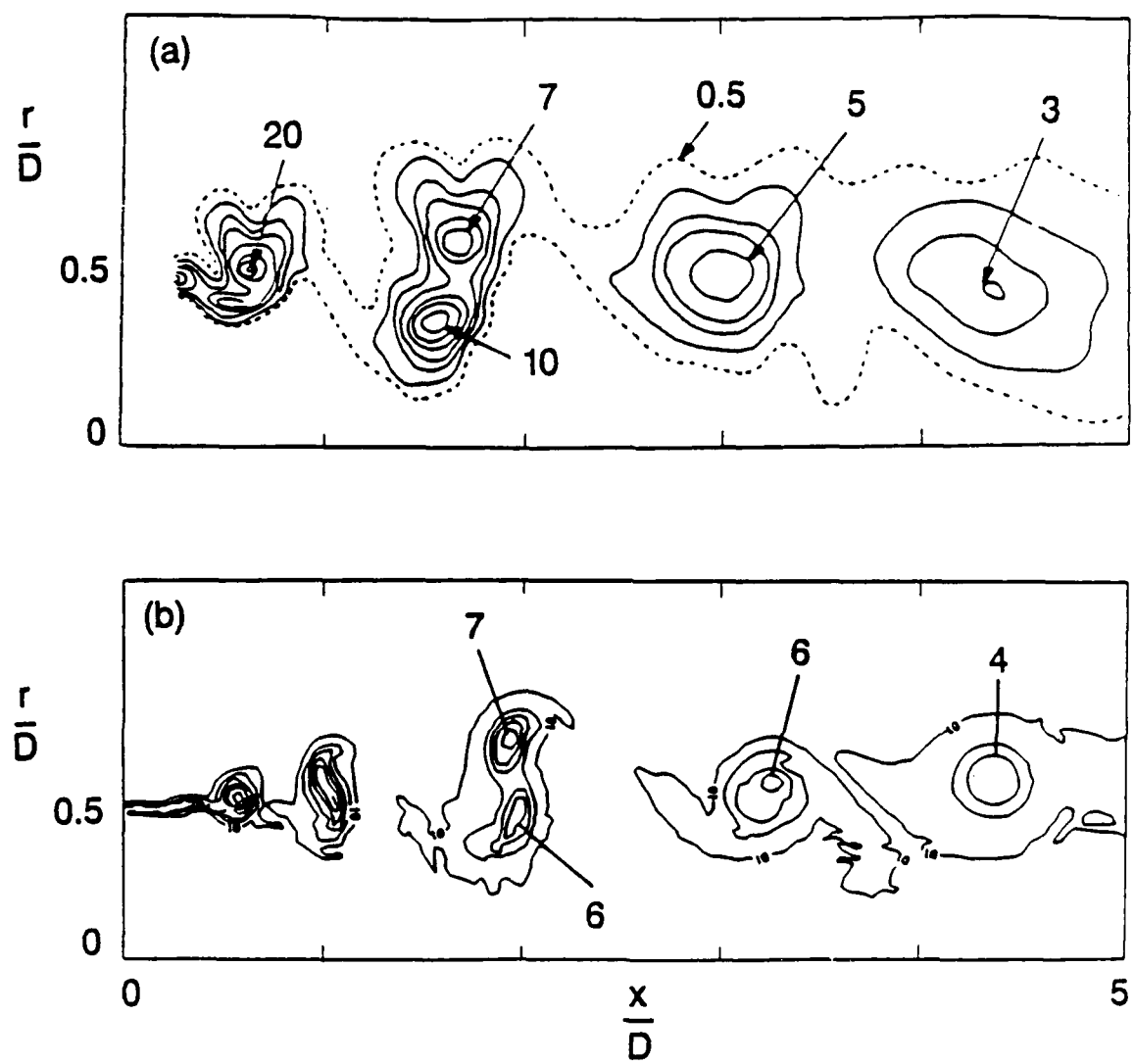
Figure 14

a) Coherent (phase-averaged) azimuthal vorticity, normalized with $St_D U_o / D$, Hussain (1986);

b) Instantaneous azimuthal vorticity, normalized with $St_{\theta_o} U_o / \theta_o$, present simulations. $St_{\theta_o} = 0.014$, $M = 0.57$, $D/\theta_o = 140$.
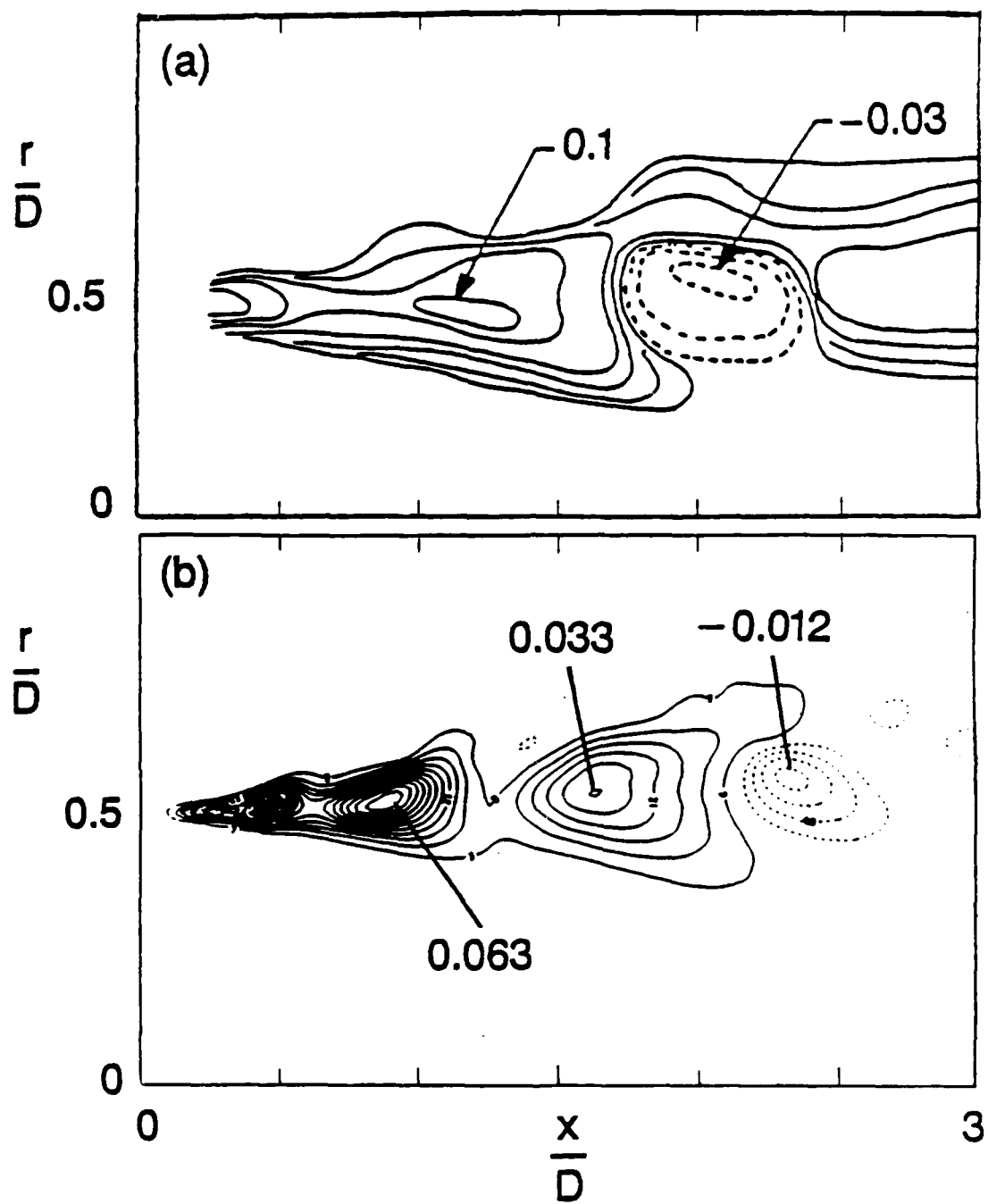
Figure 15

Turbulent kinetic energy production, full : > 0, dashed : < 0. a) $\Pi D/(0.85 U_o^3)$, Hussain (1986); b) $\Pi \theta_o/(St_{\theta_o} U_o^3)$, present simulations, $St_{\theta_o} = 0.014$, $M = 0.57$, $D/\theta_o = 140$, $\Delta_{full} = 0.006$, $\Delta_{dashed} = 0.003$.

36
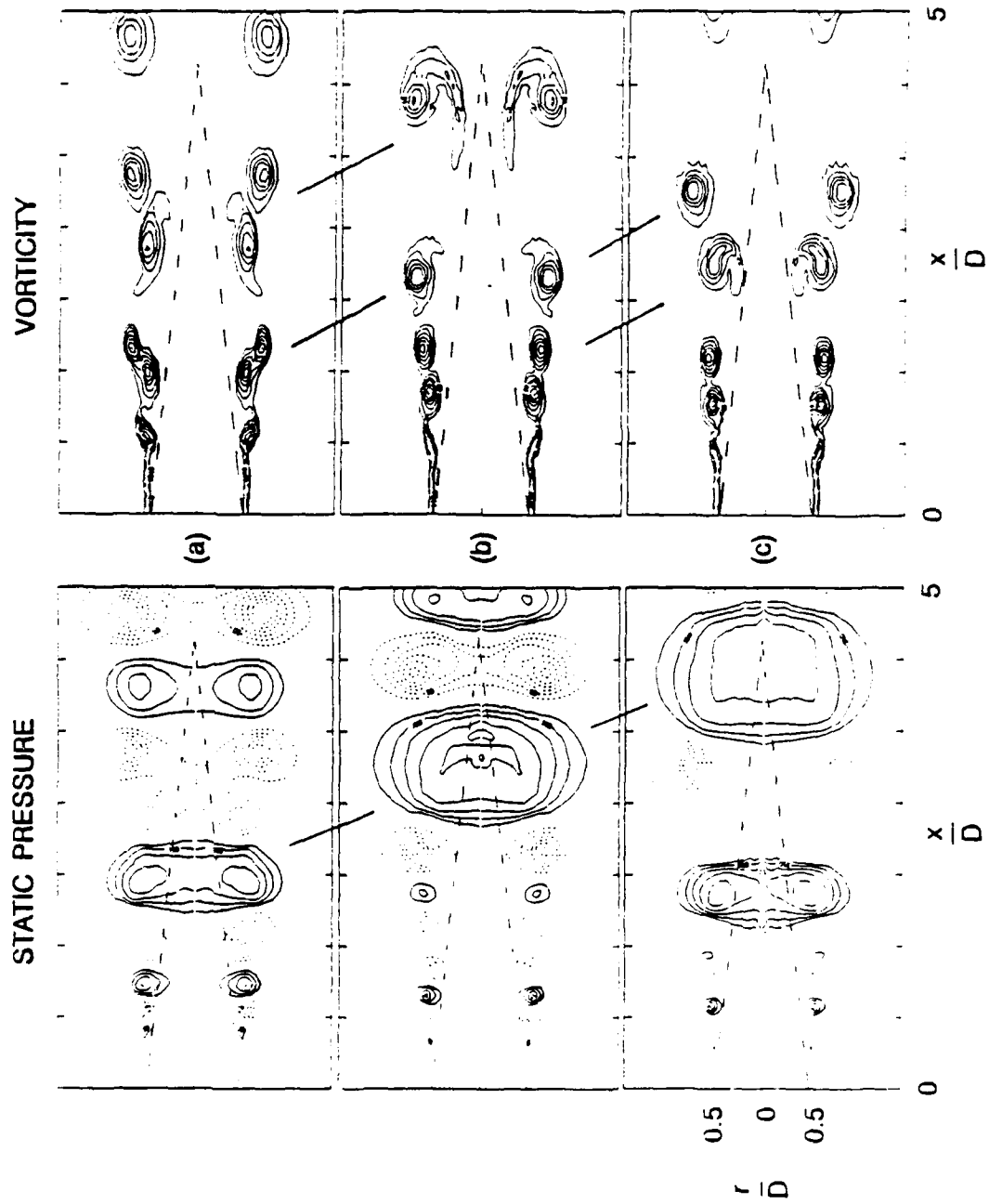
Figure 16

Jet with $M = 0.57, D/\theta_o = 70$; Instantaneous azimuthal vorticity, $\Omega/f_o, \Delta = 1.75$; Instantaneous relative static-pressure difference, $(\overline{P} - P_{amb})/P_{amb}, \Delta = 0.025$, full : > 0, dashed : < 0.

37

MAXIMUM P

MINIMUM P
MAXIMUM Ω
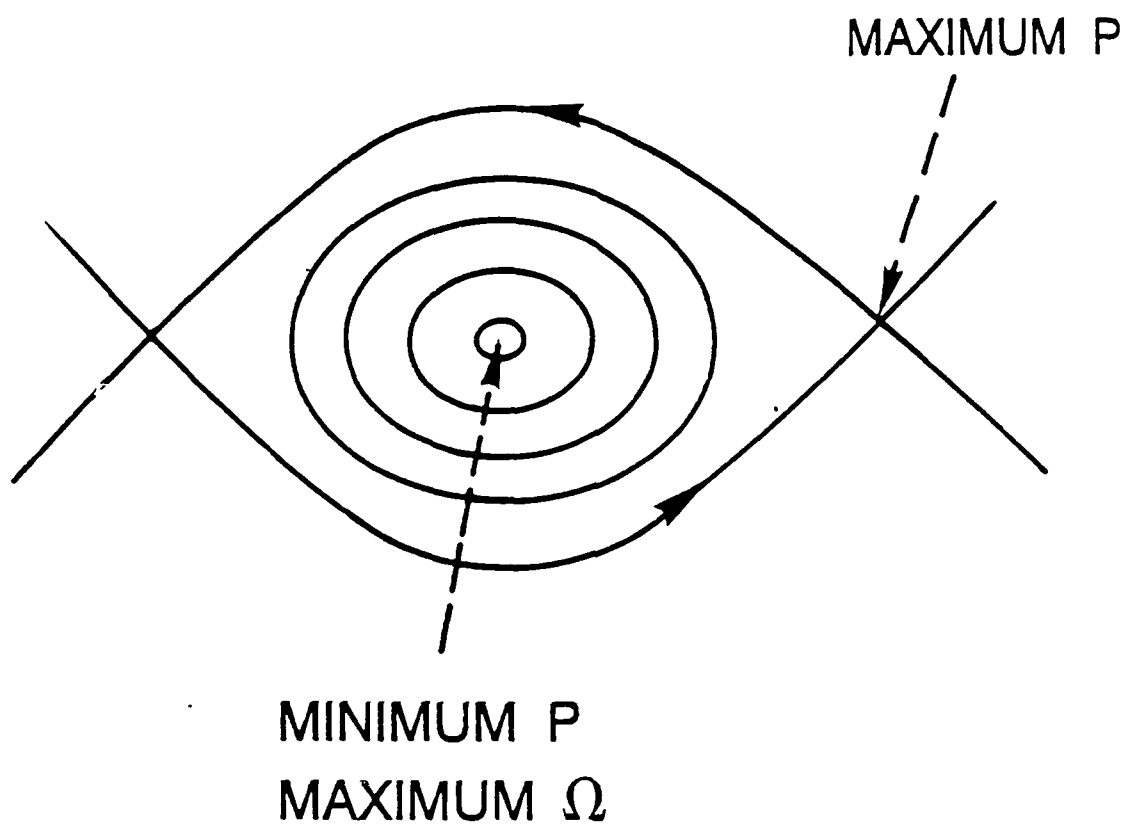
Figure 17

Schematic of a vortex-ring cross-section.
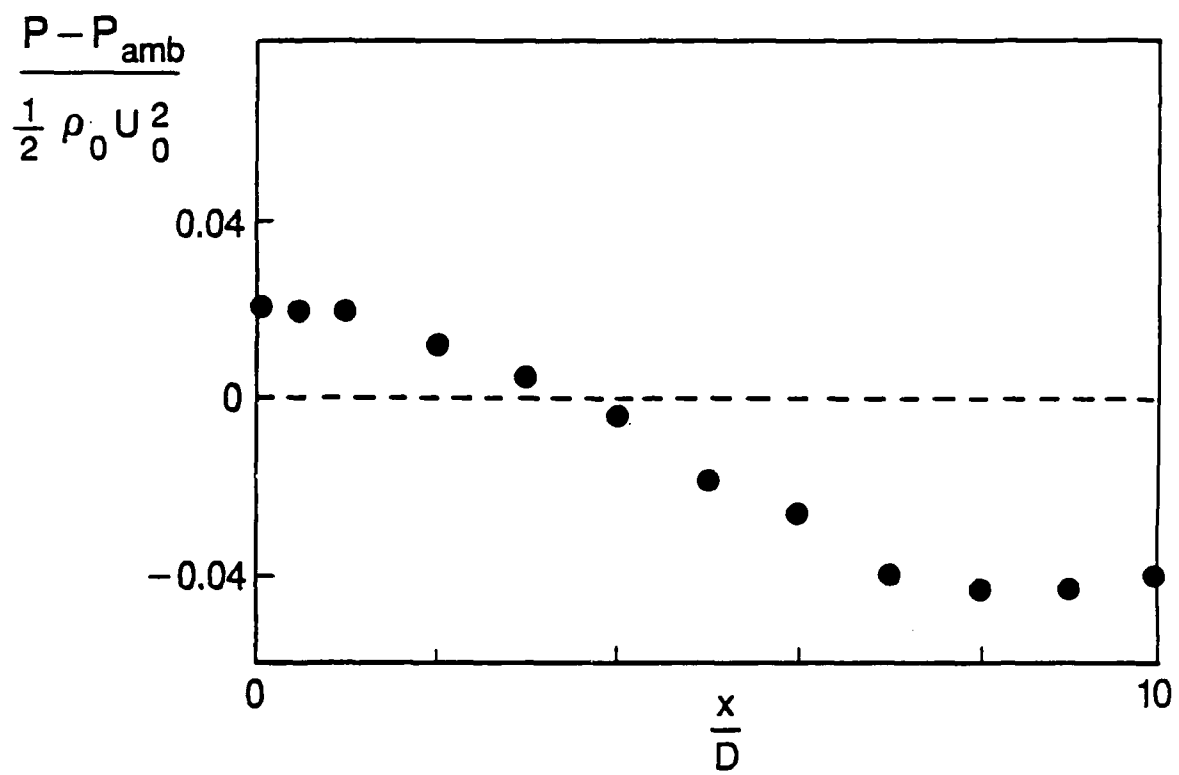
Figure 18

Mean static pressure along the centerline for a circular jet, Toyoda and Hussain (1987).

39
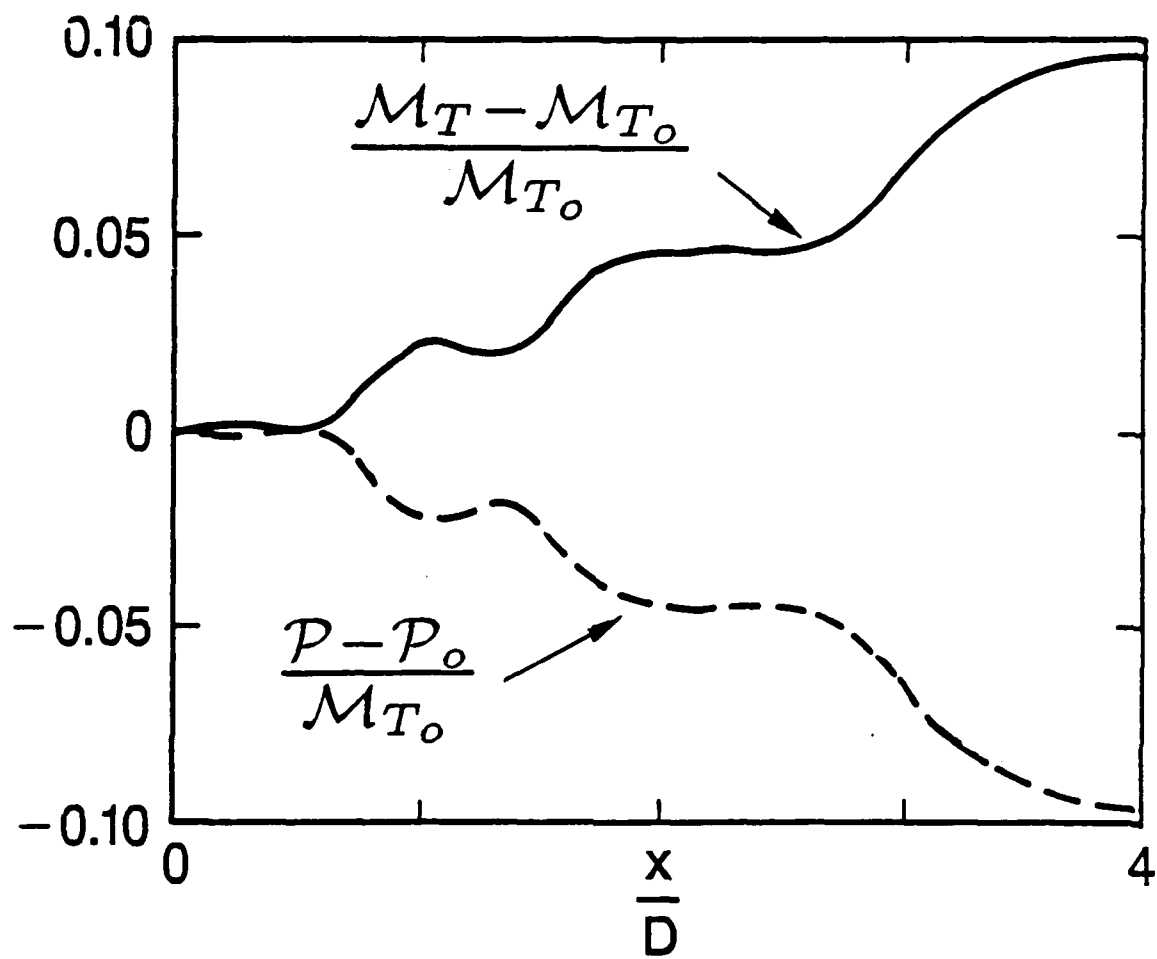
Figure 19

Balance between the streamwise momentum flux and the mean integrated pressure in the case $M = 0.57, D/\theta_o = 70$; full : $.\frac{\mathcal{M}_T(x) - \mathcal{M}_T(x_o)}{\mathcal{M}_T(x_o)}$, dashed : $\frac{\mathcal{P}(x) - \mathcal{P}(x_o)}{\mathcal{M}_T(x_o)}$.
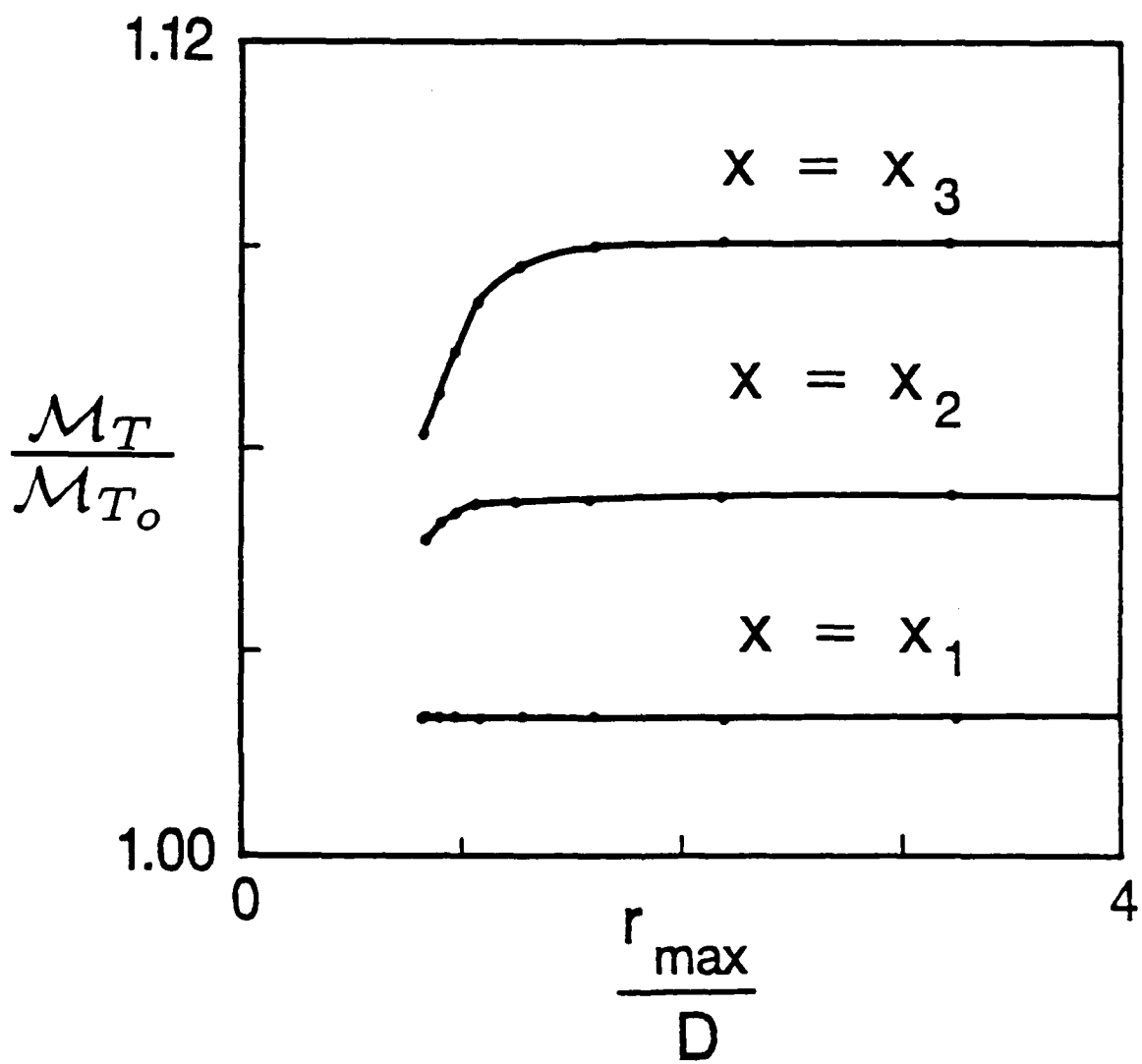
Figure 20

Dependence of $\mathcal{M}_T(x)$ on the radial cutoff used to evaluate numerically the integral in eq. 8.
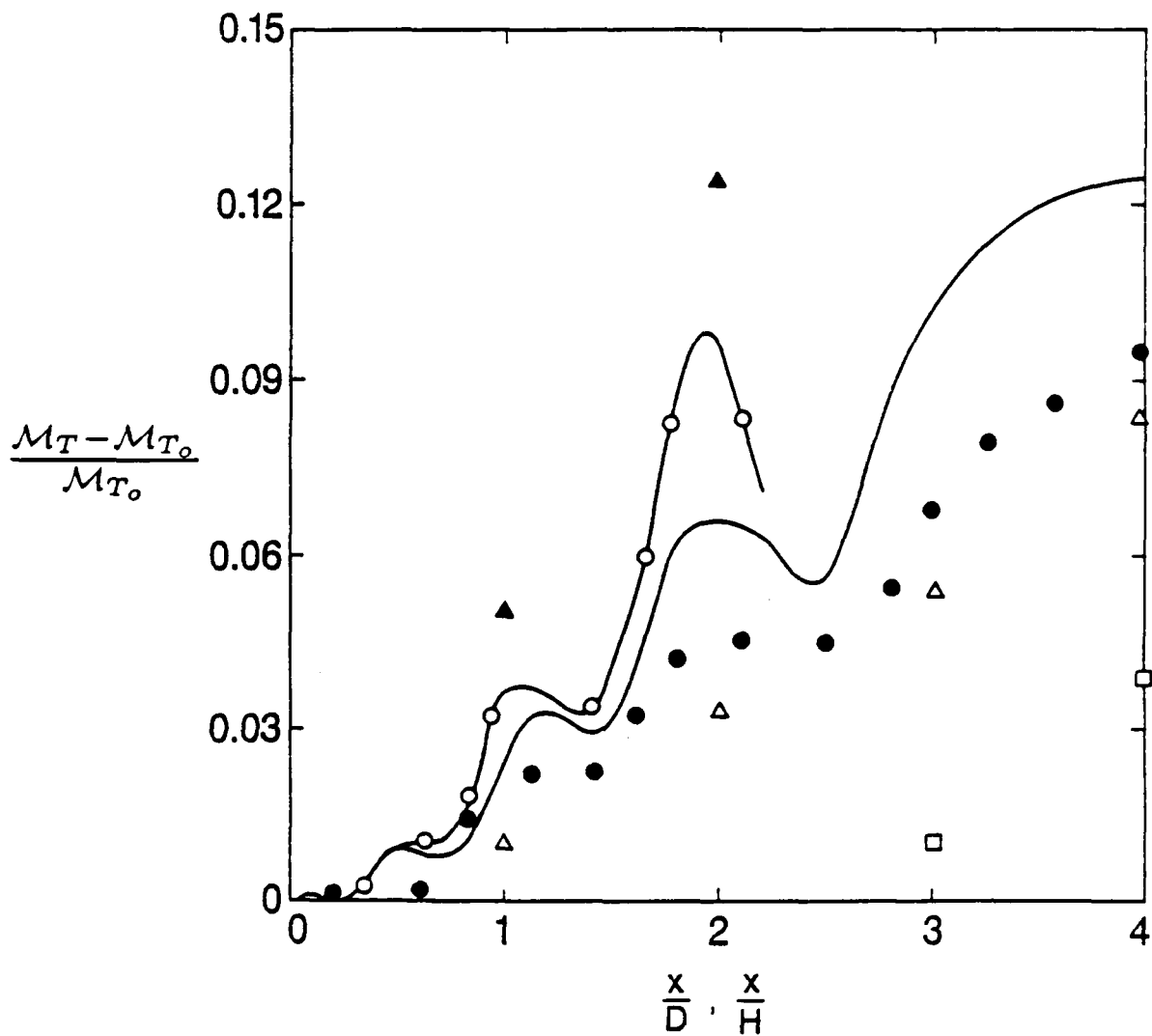
Figure 21

Streamwise momentum flux increase. —— : $U_o = 2.0 \times 10^4 \ cm/s \ (M = 0.57), D/\theta_o = 140$: ● : $U_o = 2.0 \times 10^4 \ cm/s \ (M = 0.57), D/\theta_o = 70$: –O–: $U_o = 1.5 \times 10^4 \ cm/s \ (M = 0.43), D/\theta_o = 140$; $\triangle$: planar jet, $U_o = 3.8 \times 10^3 \ cm/s$, Hussain and Clark (1978); ▲: planar jet. $U_o = 1.5 \times 10^3 \ cm/s$, Hussain and Clark (1978); ◻: circular jet. $U_o = 3.8 \times 10^3 \ cm/s$. Crow and Champagne(1971).
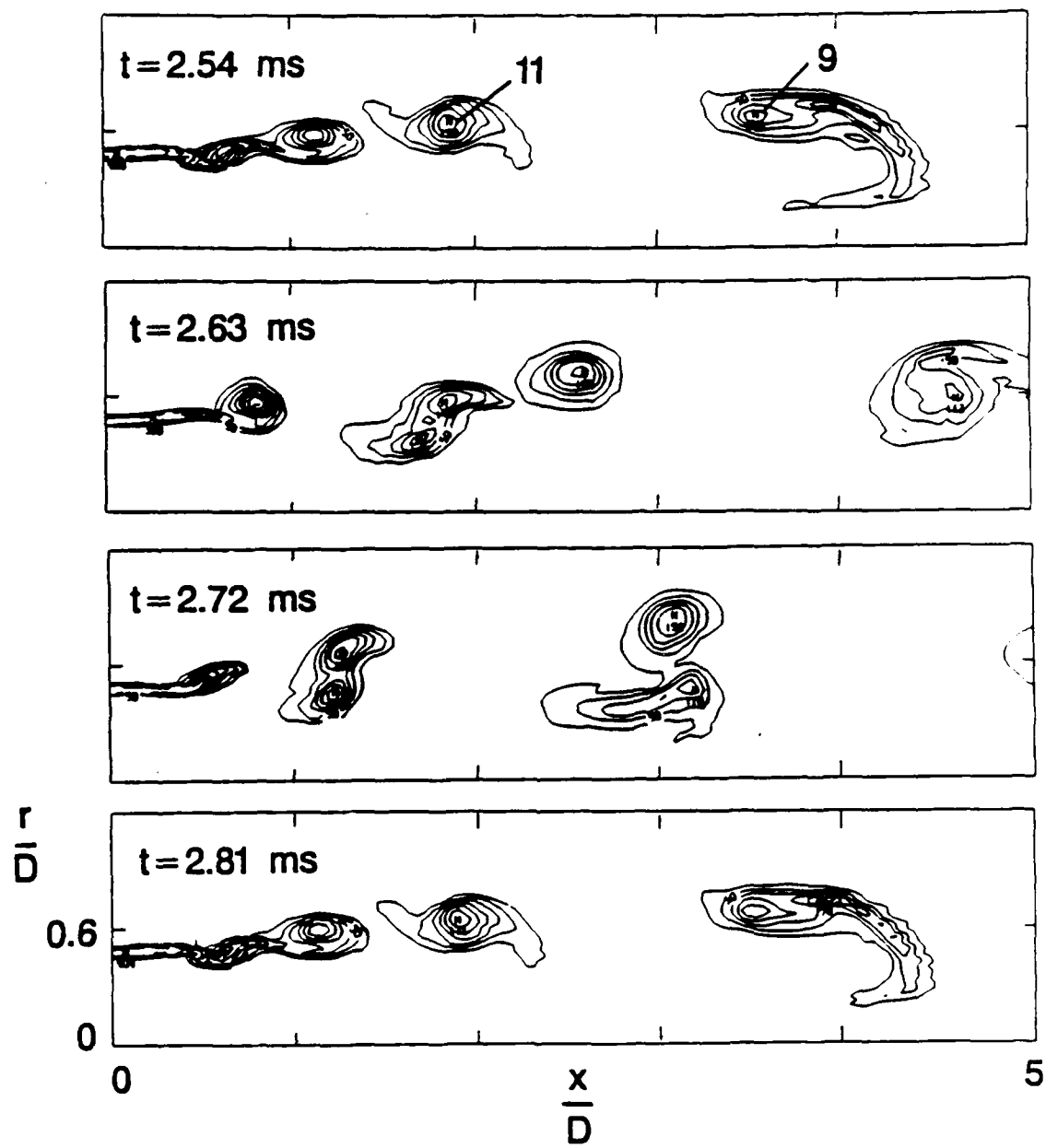
Figure 22

Instantaneous azimuthal vorticity, Ω/f_o, $\Delta = 1.8$, shear-layer instability mode. $M = 0.57$, $D/\theta_o = 70$.
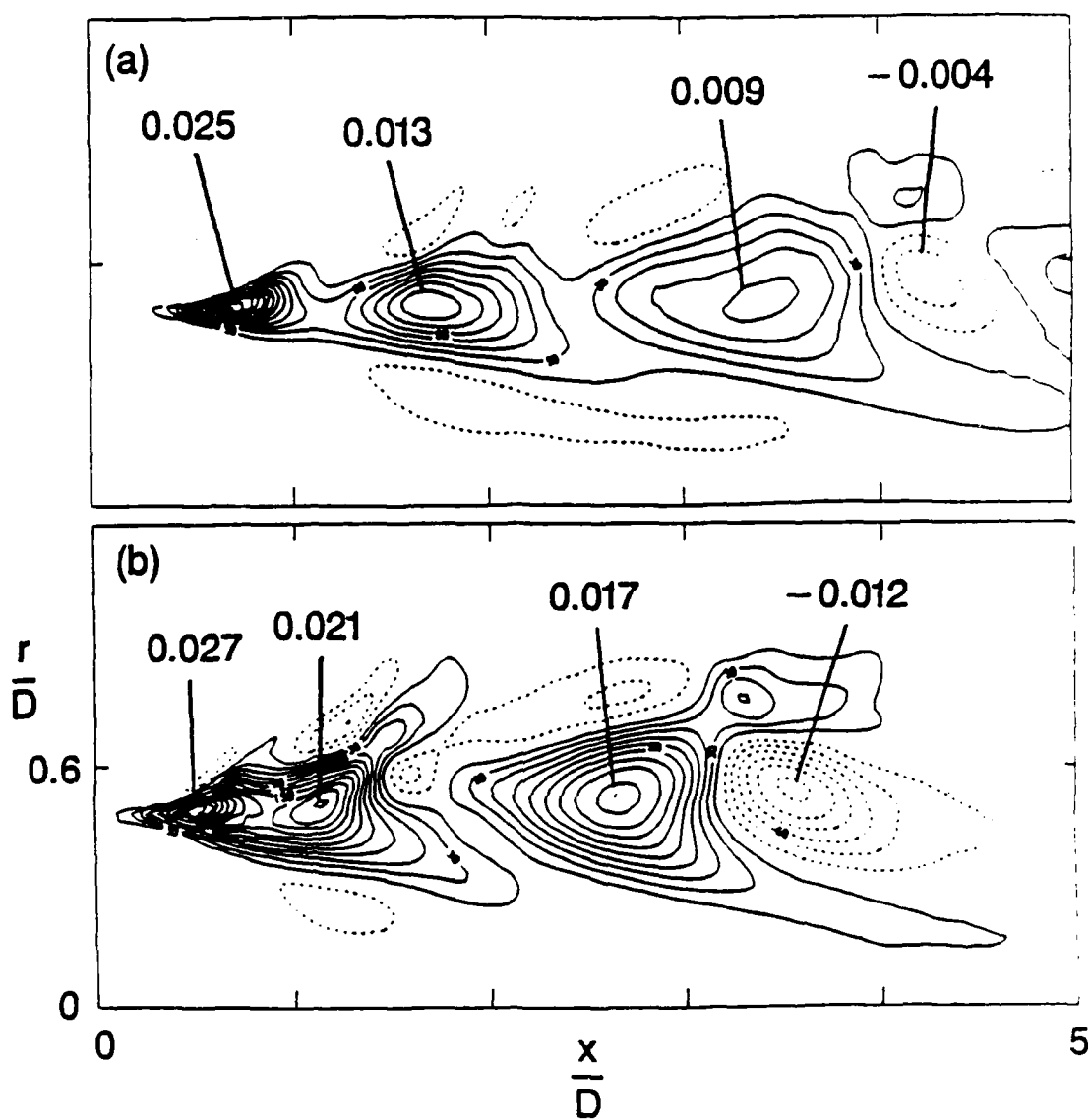
Figure 23

Reynolds stress, $M = 0.57, D/\theta_o = 70, \Delta = 0.002$; full : > 0, dashed : < 0; a) unexcited; b) shear-layer instability mode.
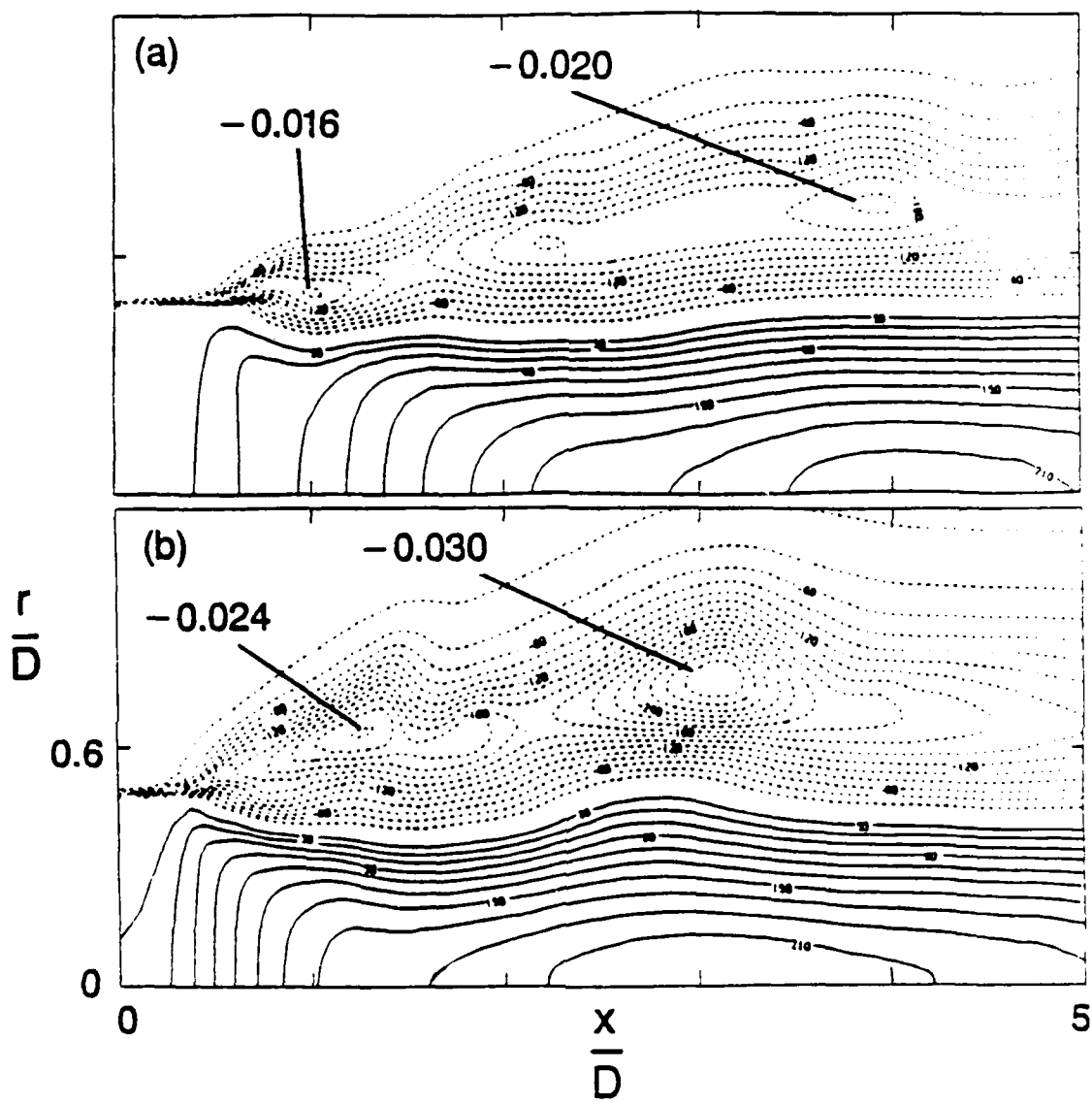
Figure 24

Mean relative static pressure. $(\overline{P} - P_{amb})/P_{amb}$, $\Delta = 0.002$. $M = 0.57$, $D/\theta_o = 70$; full : > 0, dashed : < 0; a) unexcited; b) shear-layer instability mode.
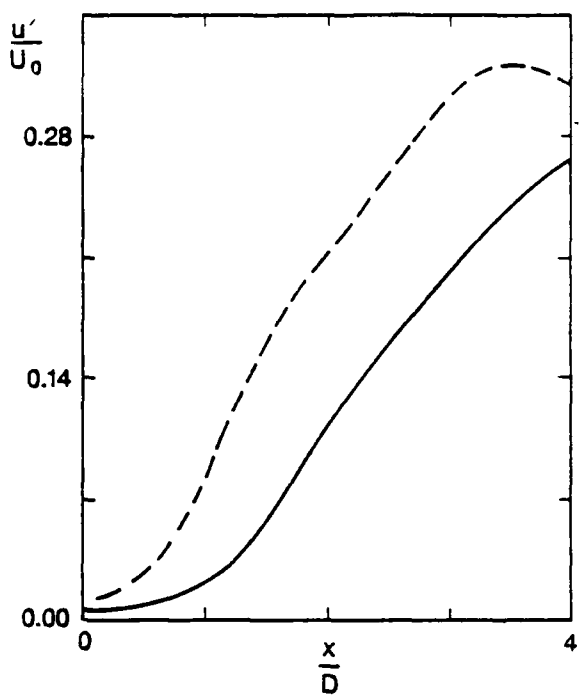
(a)
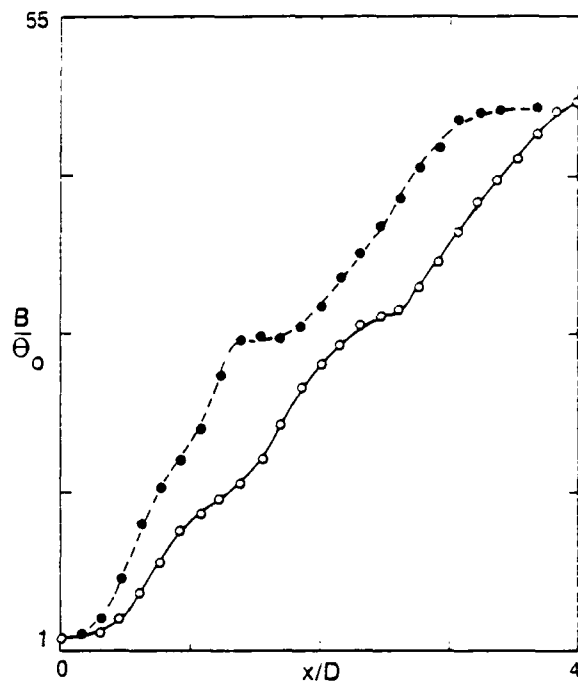
(b)
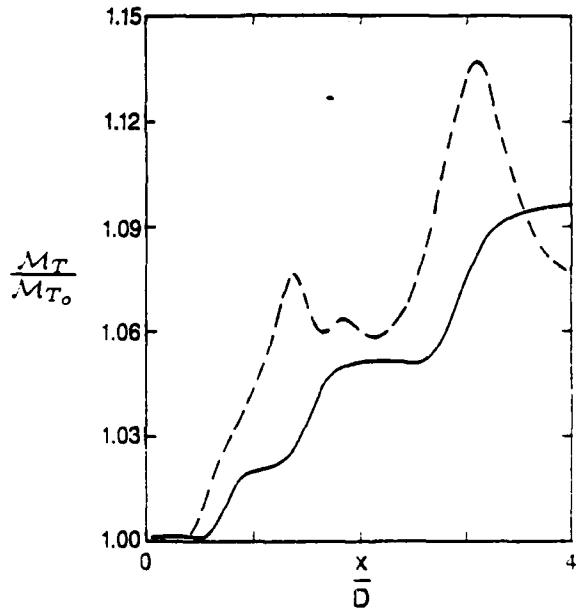
(c)

Figure 25

Streamwise variation of time-averaged flow measures as a function of controlled excitation. Case $M = 0.57, D/\theta_o$. a) u'/U_o; b) B/θ_o; c) $\mathcal{M}_T/\mathcal{M}_{T_o}$; full : unexcited, dashed : excited.
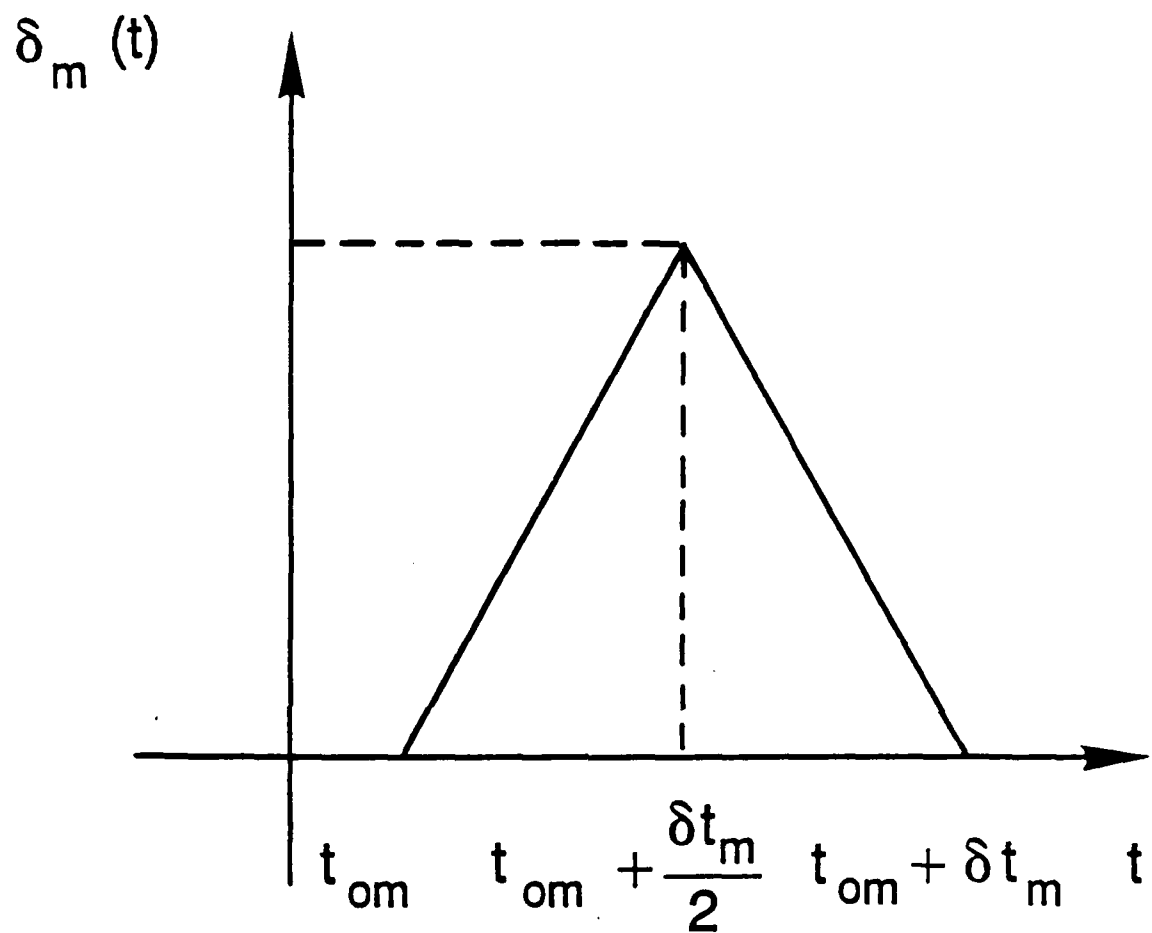
Figure 26

Time-dependent amplitude for the random inflow velocity perturbations.

REFERENCES

Abramovich, G.N. 1963, The Theory of Turbulent Jets, MIT Press.

Ashurst, W.T 1979, in Turbulent Shear Flows I, Springer-Verlag, ed. by F. Durst et al., pp. 402-413.

Boris, J.P. and Book, D.L. 1976, in Methods in Computational Physics, Vol. 16, pp. 85-129, Academic Press, New York.

Boris, J.P., Oran, E.S., Fritts, M.J., & Oswald, C.E. 1983, Time-Dependent, Compressible Simulations of Shear Flows: Tests of Outflow Boundary Conditions, NRL Memorandum Report 5249, Naval Research Laboratory, Washington, DC.

Boris, J.P., Oran, E.S., Gardner, J.H., Grinstein, F.F. and Oswald, C.E. 1985, in *Ninth International Conference on Numerical Methods in Fluid Dynamics*, ed. by Soubbaramayer and J.P. Boujot, pp. 98-102, Springer Verlag, New York.

Bradbury, L.J.S. 1965, The Structure of a Self-Preserving Turbulent Plane Jet, *J. Fluid Mech.* 23, 31.

Browand, F.K. and Ho, C.M. 1983, The Mixing Layer: An Example of Quasi Two-Dimensional Turbulence, *J. Mécanique Théorique et Appliquée*, Numéro Spécial, 99-120.

Clark, A.R. 1974, Effect of Initial Conditions on the Development of a Plane Turbulent Jet, MS Thesis, U. of Houston.

Corcos, G.M. 1980, in The Role of Coherent Structures in Modelling Turbulence and Mixing, ed. by J. Jimenez, Springer Verlag, pp. 10-40.

Davis, R. W. and Moore, E. F. 1985, A Numerical Study of Vortex Merging in Mixing Layers, *Phys. Fluids* 28, 1626.

Gaster, M. 1962, A Note on the Relation Between Temporally-Increasing and Spatially-Increasing Disturbances in Hydrodynamic Stability, *J. Fluid Mech.* 14, 222-224.

Grinstein, F.F. & Guirguis, R.H. 1987, private communication, to be published.

Grinstein, F.F., Oran, E.S. and Boris 1987, J.P., Direct Numerical Simulations of Axisymmetric Jets, *AIAA J.* 25, 92-98.

Grinstein, F.F., Oran, E.S. and Boris, J.P. 1986, Numerical Simulation of Asymmetric Mixing in Planar Shear Flows, *J. Fluid Mech.* 165, 201.

Ho C.M. and Huang L.S. 1982, Subharmonics and Vortex Merging in Mixing Layers, *J. Fluid Mech.* 119, 443.

Ho C.M. and Huerre P. 1984, Perturbed Free Shear Layers, *Ann. Rev. Fluid Mech.* 16, 365.

Husain, Z.D. 1981, An Experimental Study of the Effects of Initial and Boundary Conditions on Near and Far Fields of Jet Flows, PhD Thesis, Univ. of Houston.

Husain, Z.D., and Hussain, A.K.M.F. 1983, Natural Instability of Free Shear Layers, *AIAA J.* 21. 1512.

Hussain A.K.M.F. and Clark A.R. 1977, Upstream Influence on the Near Field of a Plane Turbulent Jet, *Phys. Fluids* 20, 1416.

Hussain, A.K.M.F. and Zaman, K.B.M.Q. 1978, The Free Shear Layer Tone Phenomenon and Probe Interference, *J. Fluid Mech.* 87, 349–383.

Hussain, A.K.M.F., and Zedan, M.F. 1978, Effects of the Initial Condition on the Axisymmetric Free Shear Layer: Effect of the initial Fluctuation Level, *Phys. Fluids* 21. 1475–1481.

Hussain, A.K.M.F., Husain, H.S., Zaman, K.B.M.Q., Tso, J., Hayakawa, M., Takaki, R., and Hasan M.A.Z. 1986, Free Shear Flows: Organized Structures and Effects of Excitation. AIAA Paper 86-0235.

Hussain, A.K.M.F. 1983, Coherent Structures–Reality and Myth, *Phys. Fluids* 26, 2816–2850.

Hussain, A.K.M.F. 1986, Coherent Structures and Turbulence, *J. Fluid Mech.* 173, 303–356.

Kailasanath, K., Gardner, J., Boris, J., and Oran, E. 1987, Interactions Between Acoustics and Vortex Structures in a Central Dump Combustor, *J. Prop. Power.* 3, 525-533.

Kibens, V. 1979, Discrete Noise Spectrum Generated by an Acoustically Excited Jet, *AIAA J.* 18, 434.

Kline, S.J., Coles, D.E., Eggers, J.M. & Harsha, P.T. 1973, NASA SP-321, p. 655.

Maestrello, L. and McDaid., E. 1971, Acoustic Characteristics of a High Subsonic Jet, *AIAA J.* 9, 1058.

Metcalfe, R.W., Hussain, A.K.M.F., & Menon, S. 1987, in Turbulent Shear Flows 5. ed. by F. Durst et al., pp. 110-123 Springer Verlag.

Michalke, A. 1965, On Spatially Growing Disturbances in an Inviscid Shear Layer, *J. Fluid Mech.* 23, 521–544.

Miller, D.R. and Comings, E.W. 1957, Static Pressure Distribution in the Free Turbulent Jet. *J. Fluid Mech.* 3, 1.

Moin, P., Rogers, M.M., and Moser, R.D. 1985, Structure of Turbulence in the Presence of Uniform Shear, Proc. of the Fifth Symposium on Turbulent Shear Flows, Cornell University, pp. 17:21–26.

Mons, R.F. & Sforza, P.M. 1971, Polytechnic Institute of Brooklyn, PIBAL Report No. 71-14.

Oran, E.S. & Boris, J.P. 1987, Numerical Simulation of Reactive Flow. Elsevier.

Oster, D. and Wygnanski, I 1982. *The forced mixing layer between parallel streams. J. Fluid Mech.* 123. 91–130.

Patnaik, P.C., Sherman, F.S., and Corcos, G.M. 1976. A Numerical Simulation of Kelvin-Helmholtz Waves of Finite Amplitude. *J. Fluid Mech.* 73, 215.

Patnaik, G., Guirguis, R.H., Boris, J.P., and Oran, E.S. 1987, A Barely Implicit Correction for Flux Corrected Transport, *J. Comp. Physics* 71, 1-20.

Riley, J.J. and Metcalfe, R.W. 1980, Direct Numerical Simulation of a Perturbed Turbulent Mixing Layer, AIAA Paper 80-0274.

Sami, S., Carmody, T., and Rouse, H. 1967, Jet Diffusion in the Region of Flow Establishment, *J. Fluid Mech.* 27, 231.

Schlichting, H. 1968, Boundary Layer Theory, McGraw Hill, pp. 174-175.

Toyoda, K. 1986, private communication

Zaman, K.B.M.Q., and Hussain, A.K.M.F. 1977, in *Proceedings of Symposium on Turbulent Shear Flow*, Penn. State Univ., pp. 11:23-11:31.

Zaman, K.B.M.Q., and Hussain, A.K.M.F. 1980, Vortex Pairing in a Circular Jet Under Controlled Excitation. Part 1. General Jet Response, *J. Fluid Mech.* 101, 449.